CHAPTER III

SELF-ASSEMBLED NANOSTRUCTURES

Nanotechnology deals with materials and systems having dimensions in the order of a billionth of a meter (1×10^{-9}). There are two methods of nanofabrication: top-down and bottom-up methods. The top-down method includes lithographic patterning and etching techniques, which are complicated and the crystal quality of nanostructure is low. On the contrary, self-assembled nanostructures by bottom-up methods such as MBE and MOCVD can give defects-free and high-quality nanostructures. This leads many researchers to experimentally and theoretically investigate SAQDs. Due to the significance of SAQDs, it is important to understand their nature and characteristics, which are the main purpose of this chapter.

The organization of this chapter is as follows: the nature of low-dimensional nanostructure and the basic concepts of self assembly of nanostructures are presented in section 3.1, followed by 3.2 which describes the details of self-assembled growth, particularly the SK growth mode, material consideration, thermodynamic and kinetic analyses. In section 3.3, defects and dislocations in strained semiconductor heterostructures are considered due to their importance for the nucleation of SAQDs. Finally, in section 3.4, several methods and techniques related to the growth of ordered QDs are reviewed.

3.1 Nature of Low-Dimensional Nanostructures

In bulk semiconductors, electrons are free to move in all directions, thus there is no quantum confinement. In order to achieve quantum confinement, the dimensions must be reduced. For examples, if one degree of freedom is removed, a quantum well is obtained; if two, a quantum wire; and if three, a quantum dot (QD). The confinement results in a discrete atomic-like density of states (Reed et al., 1988). The required size of material to observe quantum confinement corresponds to the de Broglie wavelength. When the size of the crystal is limited in the order of the de Broglie wavelength, size quantization effect will be observed because the dimension of the crystal becomes comparable to the mean free path or the de Broglie wavelength

of carriers which in turn depends on the effective mass of the carrier (m_{eff}) and on the temperature, T: (Bimberg et al., 1999)

$$\lambda = \frac{h}{p} = \frac{h}{\sqrt{3m_{eff}k_BT}} \tag{3.1}$$

where h is the Planck's constant, p is the carrier momentum and k_B is the Boltzmann's constant. A schematic diagram showing a size comparison between bulk material, waveguide, a quantum dot and an atom is illustrated in Fig. 3.1.

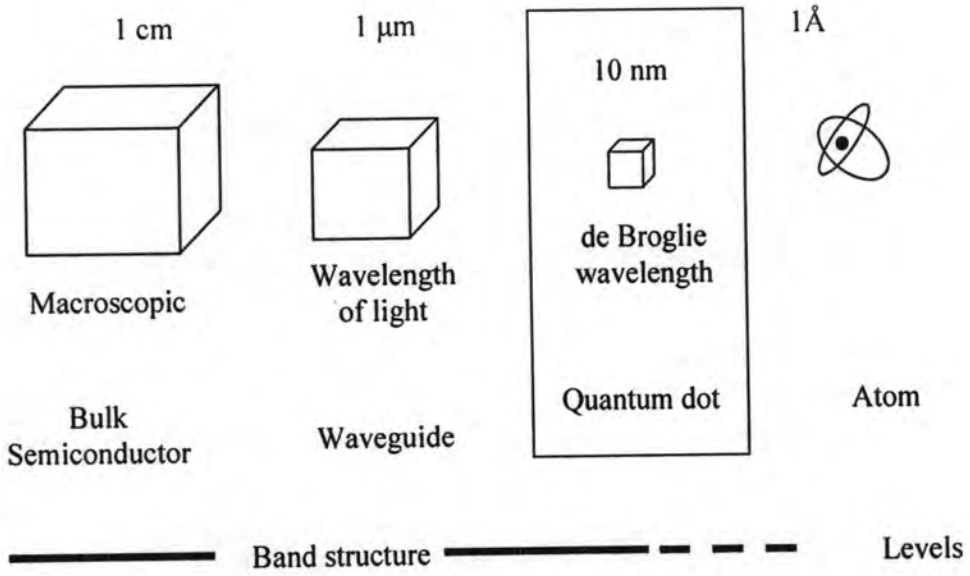

Figure 3.1 Schematic comparison of typical dimensions of bulk material, waveguide for visible light, a QD and an atom (Bimberg et al., 1999).

From Fig. 3.1, the carriers confined in the QD are quantized and resulted in discrete energy levels like an atom. Therefore, QD is sometimes called an artificial atom. The energy levels can be controlled by changing the size and shape of the quantum dot, and the depth of the potential. Fig. 3.2 shows the nature of electronic states in bulk material, quantum well and quantum dot. The charge carriers in these structures are localized to varying degrees, resulting in the possibility of quantization of energy and variations of density of states. The carrier energy (E) for bulk, quantum

well (QW), quantum wire (QWR) and QD can be expressed as follows: (Sugawara, 1999)

$$E_{bulk} = E(\mathbf{k}) = \frac{\hbar^2 k^2}{2m^*} \tag{3.2}$$

$$E_{QW} = E(\mathbf{k}) = \frac{\hbar^2 k_{//}^2}{2m^*} + E_{n,z} \tag{3.3}$$

$$E_{QWR} = E(\mathbf{k}) = \frac{\hbar^2 k_{\perp}^2}{2m^*} + E_{m,y} + E_{n,z} \tag{3.4}$$

$$E_{QD} = E_{l,x} + E_{m,y} + E_{n,z} \tag{3.5}$$

where $\mathbf{k}$= (k_x, k_y, k_z) is the wave vector of carriers, $k^2 = k_x^2 + k_y^2 + k_z^2$, $k_{//}^2 = k_x^2 + k_y^2$ and $k_{\perp}^2 = k_x^2$. The energies $E_{l,x}$, $E_{m,y}$, $E_{n,z}$ are functions of potential and depend on the quantum numbers l, m and n.

The density of states (D) for bulk, QW, QWR and QD can be expressed as follows:

$$D_{bulk}(E) = \frac{1}{2\pi^2}\left(\frac{2m^*}{\hbar^2}\right)^{3/2} E^{1/2} \tag{3.6}$$

$$D_{QW}(E) = \frac{m^*}{\pi\hbar^2}\sum_n \Theta(E - E_{n,z}) \tag{3.7}$$

$$D_{QWR}(E) = \frac{N_{wi}}{\pi}\frac{\sqrt{2m^*}}{\hbar}\sum_{m,n}\frac{1}{\sqrt{E - E_{m,y} - E_{n,z}}} \tag{3.8}$$

$$D_{QD}(E) = 2N_D\sum_{l,m,n}\delta(E - E_{l,x} - E_{m,y} - E_{n,z}) \tag{3.9}$$

where Θ is the Heaviside's unit step function, N_{wi} is the area density of the quantum wire, δ is the delta function, and N_D is the volume density of the QD.

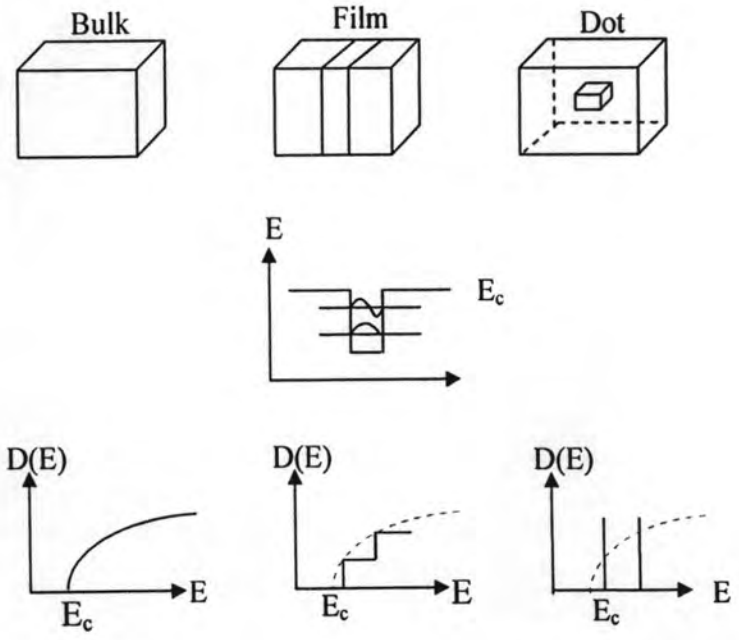

Figure 3.2 Nature of electronic states in bulk, quantum well and quantum dot. Top row: schematic morphology, center row: quantized electronic states, bottom row: density of electronic states (Bimberg et al., 1999).

Being zero dimensional, quantum dots have a sharper density of states (delta-function-like) than higher-dimensional structures as shown in Fig. 3.2. As a result, they have better transport and optical properties, and are being used in diode lasers and amplifiers. Lasing oscillation in the QD laser has been achieved at room temperature (Koichi et al., 1999).

3.2 Self-Assembly of Nanostructures

Reducing the dimensionality of semiconductor structures such as zero dimensional QDs shows discrete energy spectrum of electrons and holes, which benefits basic semiconductor physics and device technology (Reed et al, 1988), since it can yield reduced cost, compact dimensions and enhanced performance for semiconductor and photonics devices. Therefore, the understanding of growth mechanisms of self-assembled nanostructures is needed. This section reviews the fundamental mechanisms and theories of the growth of self-assembled islands.

3.2.1 Self-Assembled Growth

When a lattice mismatched structure is grown on a substrate, the lattice constant of the first few monolayers (MLs) of the deposited material is forced to match that of the substrate. The change from the desired lattice constant creates strain in the deposited layer. After a few MLs, the strain in the epilayer builds up and the strain energy is released, in some circumstances, by forming small islands. These islands are zero-dimensional, and are usually referred to as self-assembled quantum dots (SAQDs).

Three possible growth modes can occur when a strained epilayer is grown on a substrate under near equilibrium conditions and these are shown in Fig. 3.3. For a small lattice-mismatched system, when the mismatch is less than or equal to 2%, the epilayer grows in a 2D layer-by-layer, or Frank-van der Merwe, growth mode as shown in Fig. 3.3(a). If the lattice mismatch is increased, the growth occurs in a 3D mode known as Stranski-Krastanow (SK) where the growth initially starts out layer-by-layer, but later develops into islands with a wetting layer (WL) formed from the first phase of growth as shown in Fig. 3.3(b). Finally, at higher lattice mismatch, islands are instantly formed and this is called Volmer-Weber growth mode as shown in Fig. 3.3(c). The nature of the change from 2D to 3D growth mode can be explained by the surface/interface free energy model (Gilmer and Grabow, 1987). If we consider the growth mode in terms of surface energies during the film deposition, we can define the change of total energy of a surface before and after deposition $\Delta\gamma$:

$$\Delta\gamma = \gamma_f + \gamma_i - \gamma_s \tag{3.10}$$

where γ_s is the substrate surface energy, γ_f is the film surface energy, and γ_i is the interface energy between the film and the substrate which includes additional energy arising from the strain between the film and the substrate.

If $\Delta\gamma < 0$, layer-by-layer growth mode arises because the atoms of the deposit material are strongly attracted to the substrate than they are to themselves. On the contrary, if $\Delta\gamma > 0$, the deposit atoms are more strongly bound to each other than those to the substrate and the growth mode known as island or Volmer-Weber mode results. Between these two modes is the SK growth mode which arises when the interface energy increases as the layer thickness increases and $\Delta\gamma$ reaches zero. In the SK

growth mode, islands are formed on top of the WL and the SK growth is sometimes called layer-plus-island growth. Because the QDs grown in this work is SK QDs, the details of SK mode are thus given more importance and explored further here.

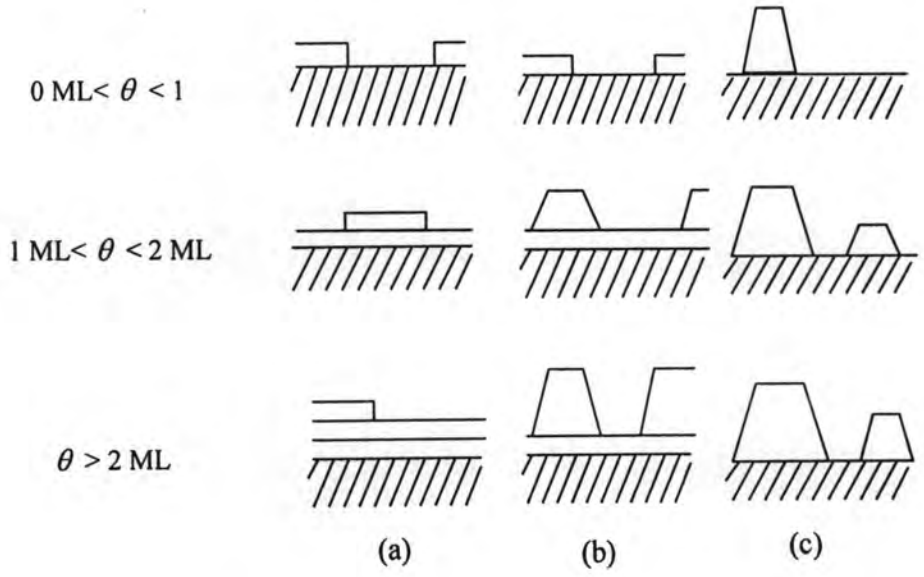

Figure 3.3 Schematic representation of the three crystal growth modes of a film for a different coverage (θ) (a) layer-by-layer or Frank-van der Merwe (b) layer-plus-island or Stranski-Krastanow mode island and (c) Volmer-Weber (Herman and Sitter, 1989).

3.2.1.1 Stranski-Krastanow Mode

Island formation in the SK growth mode is related to the accommodation of elastic strain associated with lattice mismatch. Strain relaxation in some growth conditions by the transition from platelets 2D to coherent islands 3D is explained by the elastic strain energy, *E (el),* during the growth of lattice mismatched system: (Seifert et al., 1996)

$$E(el) = \lambda \varepsilon^2 A t \qquad (3.11)$$

where λ is the elastic modulus, ε is the lattice mismatch, A is the surface area, and t is the film thickness. The elastic strain energy for layer-by-layer growth will increase linearly as a function of the deposited film volume and the energy will increase either to the point where coherent islands are nucleated, this appears as point t_{cw} in Fig. 3.4

or until it reaches the activation energy for dislocation formation, t_{cd} in the same figure.

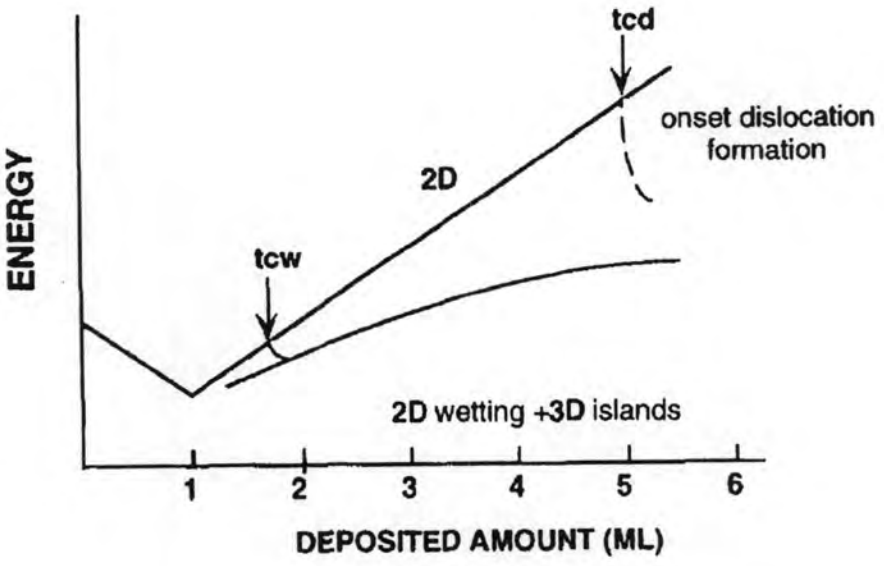

Figure 3.4 Schematic representation of total energy change for a strained system in 2D- and 3D- growth modes. t_{cw} and t_{cd} are critical thicknesses for formation of islands and dislocations, respectively (Seifert et al., 1996).

The SK growth process can be explained by Fig. 3.5 where three distinct energy periods are plotted. The first period A has two regions: the stable 2D area and the metastable 2D area, or pseudomorphic 2D layer area. At the beginning of film deposition, the stable 2D layer-by-layer growth leads to a perfect wetting of the substrate. After the film exceeds the critical wetting layer thickness (t_{cw}), 2D growth proceeds into the metastable 2D area where excess energy is stored due to the building up of a supercritical thick wetting layer.

The growth in this period continues until point X in the figure is reached beyond which the second period B sets in. Period B has two steps: island nucleation and island growth. At point X, the excess energy of the strained 2D layer reaches the energy of the 2D-3D transition barrier E_A and a pure strain-induced 2D-3D transition will take place. In other words, the nucleated islands at point X decompose the 2D layer supercritically, thus providing material for 3D island growth. As growth continues into period C, Ostwald ripening (Zinke-Allmang et al., 1987) will occur.

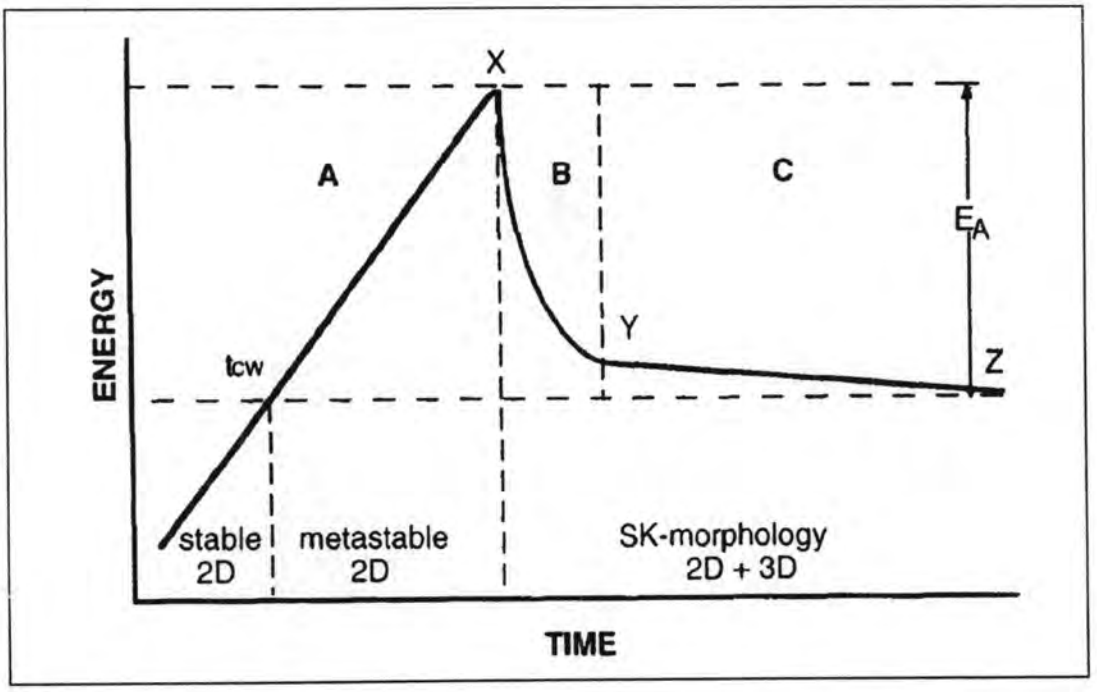

Figure 3.5 Schematic illustration of total energy as a function of time for the 2D-3D morphology transition. A: 2D layer-by-layer growth, B: 2D-3D transition, C: ripening period, t_{cw}: critical wetting layer thickness, E_A: barrier for formation of 3D islands, X: point where a pure strain-induced transition becomes possible, and between X and Y: a slow ripening process continues (Seifert et al., 1996).

3.2.1.2 Material Consideration

Self-assembled SK QDs have been studied in various semiconductors. They are grown on Si, GaAs or InP substrates. Among these three materials, GaAs and InP are direct bandgap materials and Si is indirect. Therefore, Si is useless as light emitters although it is inexpensive, while InP and GaAs find many optoelectronics applications such as laser diodes.

The epilayer of self-assembled SK QDs is required to have a larger lattice constant than those of the substrate. This limits the type of material, and, consequently, the range of energy associated with the epilayer. Therefore, material consideration is an important role for the study of self-assembled growth. Figure 3.6 shows the relationship between the lattice constant and energy gap of III-V semiconductor material systems. As seen in the figure, InAs on GaAs (or Ge on Si) is a good material system for QD studies since the lattice constant of InAs is larger than

GaAs and carrier confinement is possible since the energy gap of InAs is smaller than that of GaAs. In this work, InAs/GaAs is the main material of interest which may find applications as long-wavelength emitters. It has been shown that $In_xGa_{1-x}As$/GaAs QDs emit long-wavelength photons in the 1.3-1.55 μm region which is important for laser applications in optical communication systems (Nakata et al., 2000; Tatebayashi et al., 2001; Eliseev et al., 2001; Kovsh et al., 2003; Xu et al., 2004).

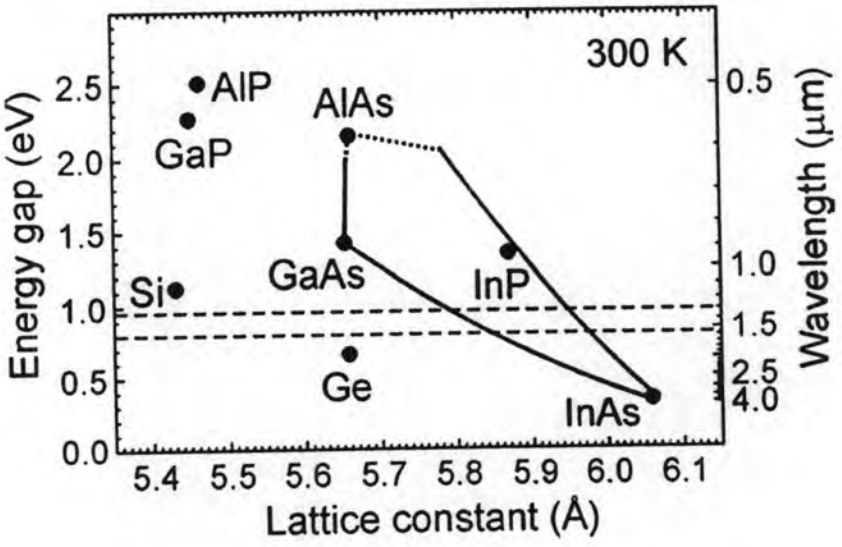

Figure 3.6 Energy gap versus lattice constant for most commonly used semiconductors.

3.2.2 Theory of Self-Assembled QD Formation

The theoretical work on self-assembled QD formation can be explained by equilibrium and nonequilibrium aspects. For the equilibrium aspects, QD formation can be explained using energetic principles and thermodynamics (Shuchukin et al., 1995; Daruka and Barabási, 1997). For the nonequilibrium aspects, QD formation can be explained using dynamical models (Dobb et al., 1997; Daruka et al., 1997). In this section, the thermodynamic and dynamical or kinetic analyses are reviewed.

3.2.2.1 Thermodynamic Analysis

The total energy of a coherently strained 3D island can be expressed in terms of elastic energy ($E_{elastic}$), surface energy (E_{surf}) and edge energy (E_{edge}) as:

$$E_{total} = E_{elastic} + E_{surf} + E_{edge} \tag{3.12}$$

Moreover, the energy per atom per unit volume in a pyramid-shaped island with a base length of L can be obtained by the sum of all the L-dependent terms as follows: (Bimberg et al., 1999)

$$E(L) = E_0\left[-2\left(\frac{L_0}{L}\right)^2 \ln\left(\frac{e^{1/2}L}{L_0}\right) + \frac{2\alpha}{e^{1/2}}\left(\frac{L_0}{L}\right)\right] \tag{3.13}$$

where E_0 and L_0 are the characteristic energy and length of the pyramid, respectively. $E(L)$ is governed by the control parameter α which is a function of the surface energy and the elastic strain energy of the island. A representative diagram for equation (3.13) is shown in Fig. 3.7.

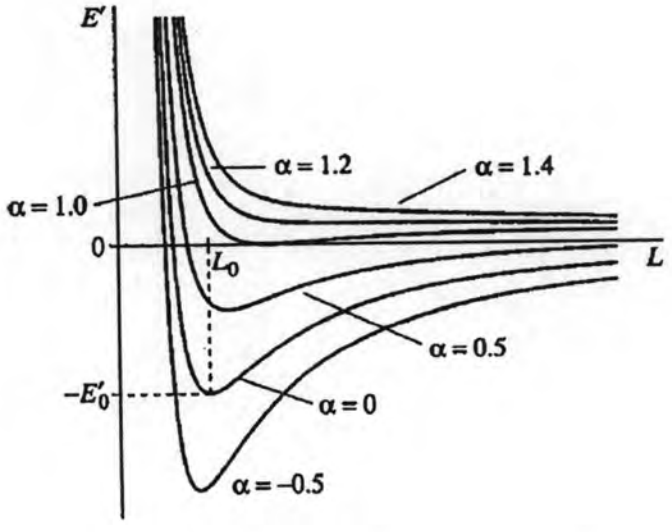

Figure 3.7 Energy of an array of 3D coherently strained islands per one atom versus size of the atom. The control parameter α is the ratio of the surface energy and edge energy (Bimberg et al., 1999).

The island is in the most stable and optimum size at the minimum energy (min $E(L) \equiv E(L_{opt})$) < 0) if $\alpha = 1$. However, the island will be ripening at the energy $E(L) \rightarrow 0$ if $\alpha \rightarrow \infty$. If $1 < \alpha < 2e^{-1/2} \approx 1.2$, the island is in a metastable state where $E(L) > 0$. Therefore, the local minimum energy $E(L)$ disappears when $\alpha > 1.2$ and there exists a thermodynamic tendency to ripen and become a single huge cluster where all the deposited materials are collected (Shchukin and Bimberg, 1999).

The investigation of the equilibrium properties of strained heteroepitaxial systems is studied by taking into account WL in order to get more understanding of the equilibrium system (Daruka and Brabasi, 1997). In their work, the desorption and interdiffusion of QD material were neglected in order to conserve the system and stored the energy in the WL with respect to the film coverage in order to minimize the energy of the system. When H ML of epilayer is deposited on a substrate, a fraction of H ML (H_1) is formed as a wetting layer and H_2 ML is distributed in the form of 3D pyramidal shaped islands. The rest of the H ML which is equal to (H-H_1-H_2) ML is assembled in the ripened islands. This implies that the growth of 3D coherent islands is initiated via the formation of 2D platelets which act as precursors. Therefore, the total energy density (total energy per unit cell) of this system is given by

$$E = H_1 E_{WL} + H_2 E_{island} + (H - H_1 - H_2) E_{rip} \qquad (3.14)$$

From the equation (3.14), the nucleation of 3D islands depends on the WL thickness, and the total volumes of all islands are not limited. The Phase diagram of lattice-mismatched system shown in Fig. 3.8 is for the understanding of the equilibrium morphology of the heteroepitaxial system. In this figure, there are six growth modes (phases) and these phases are separated by the phase boundary lines: H_{c_2}: FM-R_1, FM-SK_1; H_{c_2}: SK_1-R_2; H_{c_3}: SK_2-SK_1; H_{c_4}: VW-SK_2, VW-R_3 (Barabási, 1999).

The FM phase

In this phase, the deposited material contributes to the pseudomorphic growth of the wetting film, and the islands are absent, reminiscent of the so-called FM growth mode. The WL thickness in this case is the same as the nominal thickness of the material deposited, H. Such growth of the WL will

continue until H reaches a critical value H_{c_1}, which defines the phase boundary between the FM and either the R_1 or the SK_1 phases.

The R_1 Phase

Above H_{c_1}, but when the inequality $0 < \varepsilon < \varepsilon_1$ is satisfied after the formation of a WL of $n_1 = H_{c_1}$ ML, the excess material $(H - n_1)$ contributes to the formation of *ripening* islands.

The SK_1 phase

Above H_{c_1} and for $\varepsilon_1 < \varepsilon < \varepsilon_2$, the deposited material H is distributed between the wetting film, and finite stable islands, in a process similar to the SK growth mode. At H_{c_1} the equilibrium island size jumps from zero (in the FM phase) to some finite $x_0(H, \varepsilon)$ value. Naturally, within the SK_1 phase the island size, their mass, the WL thickness, and the island density p are continuous functions of H and ε. With increasing H, the density p increases from 0 at H_c to a finite value. Interestingly, as a consequence of island-island interactions in the SK_1 phase the WL also continues to grow, but at a sub-linear rate.

The R_2 phase

In this phase the deposited material A is distributed between a wetting film, finite islands, and ripening islands. The finite islands formed in the SK_1 phase are preserved, being stable with respect to ripening. Thus in the R_2 phase both finite stable islands and ripening islands coexist.

The VW phase

For large lattice misfits ($\varepsilon > \varepsilon_2$) and for small coverages H, *all* the deposited material is accumulated in the form of finite islands. Due to the large misfit, in this phase the wetting film is absent and the islands form directly on the substrate, similar to the so-called VW growth mode. In the absence of the wetting film, *both* the island size x_0 and the island density p simply increase with H.

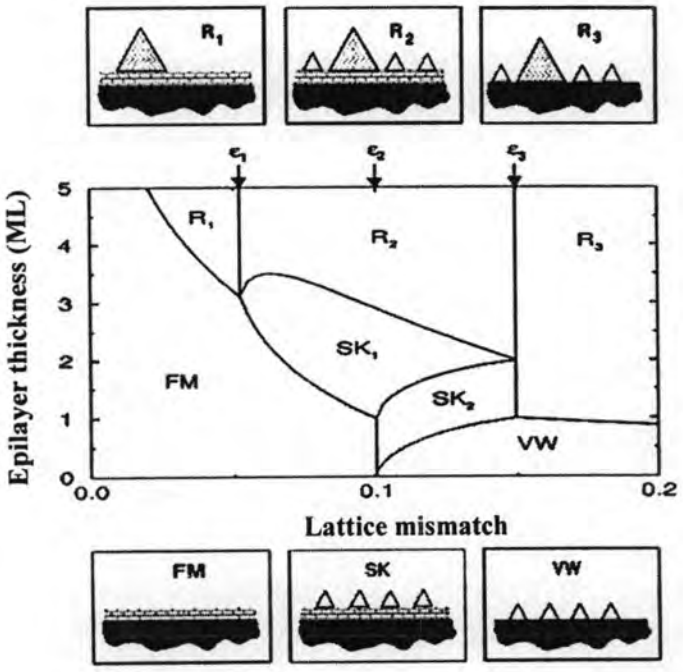

Figure 3.8 Equilibrium phase diagram of a lattice-mismatched heteroepitaxial system as a function of epilayer thickness H and the lattice mismatch. The small panels on the top and bottom illustrate the morphology of the surface in the six growth modes. The small empty triangles represent the presence of stable islands, while the large shaded area ones refer to ripened islands (Daruka and Barabási, 1997).

The SK_2 phase

By increasing H in the regime $\varepsilon_2<\varepsilon<\varepsilon_3$ we reach a new phase when H exceeds the value H_{c_4} which we label the SK_2 phase. In this phase the behavior of the system is quite different from the SK_1 growth mode, since at the H_{c_4} boundary we already have islands formed in the VW mode. As we enter the SK_2 phase by increasing H above H_{c_4}, the island density and the island size remain unchanged, but a wetting film starts to form. This process continues until a full monolayer is completed, at which point we enter the SK_1 phase. Thus, in contrast with the SK_1 phase, in the SK_2 phase the formation of new islands is suppressed until the one-monolayer-thick WL is completed.

The R_3 phase

In this last phase, which occurs for $\varepsilon > \varepsilon_3$ and for $H > H_{c_3}$ we expect the formation of ripening islands. The formation of stable islands is suppressed, and all the material deposited after H_{c_3} contributes only to the formation of new *ripening* islands, that *coexist* with the stable islands which had been formed in the VW growth mode. However, in contrast with R_2, in the R_3 phase the wetting film is absent.

The summarized solution is that the stability of the islands depends only on coverage (H) and sufficiently large coverage can enhance the possibility to ripened islands without dependence of the value of lattice mismatch (ε).

3.2.2.2 Kinetic Analysis

The kinetic model for the time-dependent 3D island density for semiconductor heteroepitaxy is explained by the island using a mean-free theory by Dobbs et al. (1997). This model describes how this density varies with growth conditions. Theoretical analysis of SK growth kinetics for the island density using growth rate equation is based on the physical processes of adatom deposition, surface diffusion, attachment and detachment of adatoms from the islands as follows: the atoms deposit and adsorb to the growing surface. The deposited atoms on the growing surface known as adatoms diffuse over the surface and collide with one another. After colliding, the adatoms form 2D islands. The small 2D islands with sizes less than critical thickness are thermodynamically unstable and quickly broken up into adatoms again. Further deposition of adatoms results in larger 2D islands. They are stable by capturing the adatoms more and transforming into 3D islands when their sizes exceed the critical sizes.

By applying the above model, the density of 3D islands formed during the deposition of InP QDs on GaP-stabilized GaAs (001) (Dobbs et al., 1997) are studied. The experimental results shows that island density increases with the growth rate and decreases with the growth temperature. It is worthy to note that the island density also increases consistently with increasing the deposition and then saturates. No significant changes in the island density for further deposition but leads to the island size. This limited size of QDs idea can also simply be explained from the self-limiting effect

proposed by Seifert et al. (1996). Many authors have already described the limited size of QDs form the kinetic aspects (Seifert et al., 1996; Chen and Washburn, 1996; Jesson et al., 1998).

Figure 3.9 illustrates the strain energy density along the surface of the WL and around an island. The change in this energy density due to the formation of 3D island affects the chemical potential. The top of the island, where the partial strain relaxation in the island takes place, is located at the minimum in the potential whereas the edge of the island, where high compressive strain exists, is at the maximum in the potential. The propagation of compressive strain at the island edge increases an inherent misfit strain between the substrate and the wetting layer around the island. The increase in the potential around the coherent island depends on the island size and so its formation has a self-limiting effect on island growth.

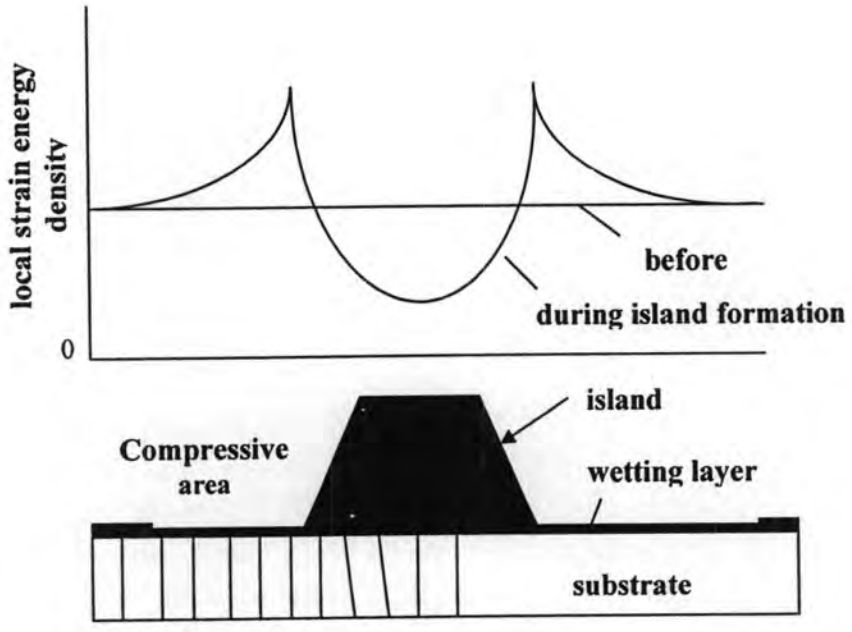

Figure 3.9 Schematic representation of the local strain energy density in and around the 3D island (Seifert et al., 1996).

3.3 Defects and Dislocations in Strained Semiconductor Heterostructures

The characteristics of a semiconductor are influenced by the strain. This section will briefly present strain in the context of semiconductor heterostructures in order to understand the strain epitaxy. The issues associated with strains such as structural

defects including point, linear and planar and volume defects in strained heterostructures are explained. Especially, the strained behaviour related to the dislocation mechanism which is one of the important matters of this work is discussed in this section.

3.3.1 Strain

When an overlayer that has a different lattice constant from a substrate is grown on the substrate, the resulting epitaxy is called a strained epitaxy. The strained behaviour of heterostructure is related to the dislocation mechanism. The main reasons why the strained heteroepitaxy is interested in are two facts. They are (i) incorporation of the built-in strain and (ii) generation of a new effective substrate. In the strained epitaxy, a thin overlayer has a built-in strain which effects on the electronic and optoelectronic properties of material. In a lattice-mismatched heterostructure, strain energy is relieved by the generation of misfit dislocations (MDs) when the overlayer thickness exceeds a critical thickness (h_c) and eventually the overlayer becomes its own substrate. This process allows the substrate possibility of growing in semiconductor technology.

The strain (ε) between the two different materials is defined by

$$\varepsilon = \frac{a_s - a_l}{a_s} \tag{3.15}$$

where a_s and a_l are lattice constants of substrate and overlayer, respectively. The accommodation of the lattice of the epitaxial layer with the substrate is shown in Fig. 3.10. In the strained heteroepitaxy, the lattice constant of the epitaxial layer in the direction parallel to the interface is forced to be equal to the lattice constant of the substrate while in the direction perpendicular to the substrate is changed by Poisson effect. Under the compressive strain, the parallel lattice constant ($a_{//}$) is forced to shrink and the perpendicular lattice constant ($a_{\perp}$) will expand. In this case, the diffraction peaks from the epilayer (at θ_e) and substrate (at θ_s) in XRD pattern are located as shown in Fig. 3.11(a) for the symmetric reflection from (00*l*) planes. Conversely, under a tensile strain, $a_{//}$ will expand and $a_{\perp}$ will shrink. In this case of smaller cubic lattice constants in a coherent epilayer, the observed diffraction peaks are shown in Fig. 3.11(b).

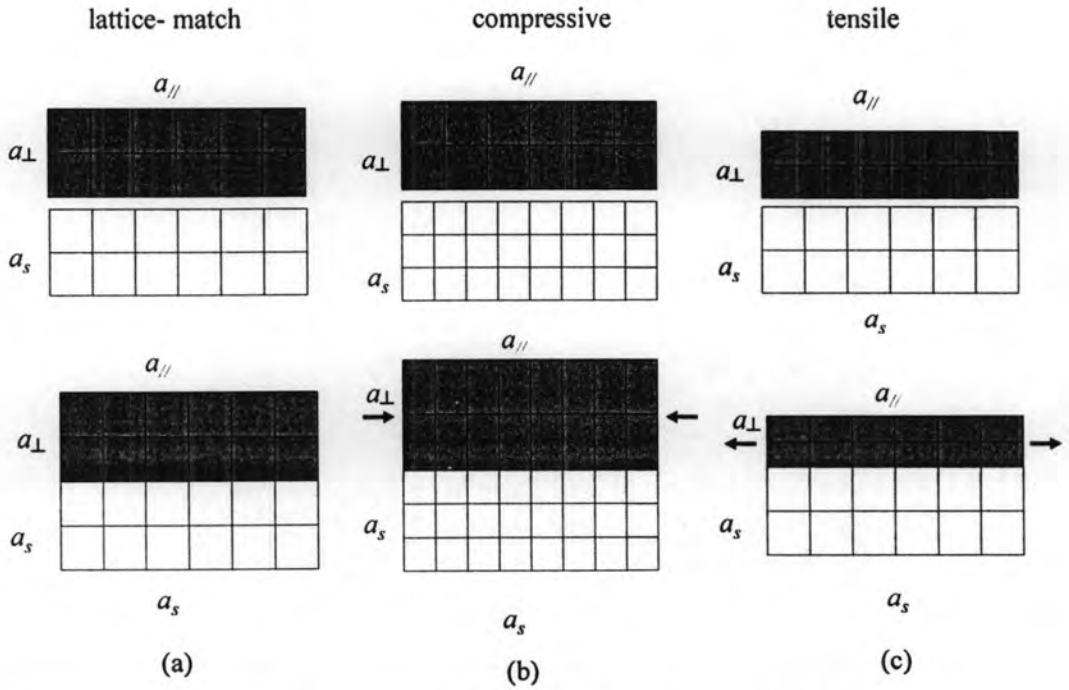

Figure 3.10 Schematic representations of (a) unstrained layer, (b) compressive strained layer and (c) tensile strained layer. The opened squares represent atoms of the substrate materials and closed squares are atoms of the epitaxial materials. In (b) and (c) the lattice constants of the epitaxial layers are different from the substrate materials. The arrows in (b) and (c) represent forces (stresses) exerted on the epitaxial layer.

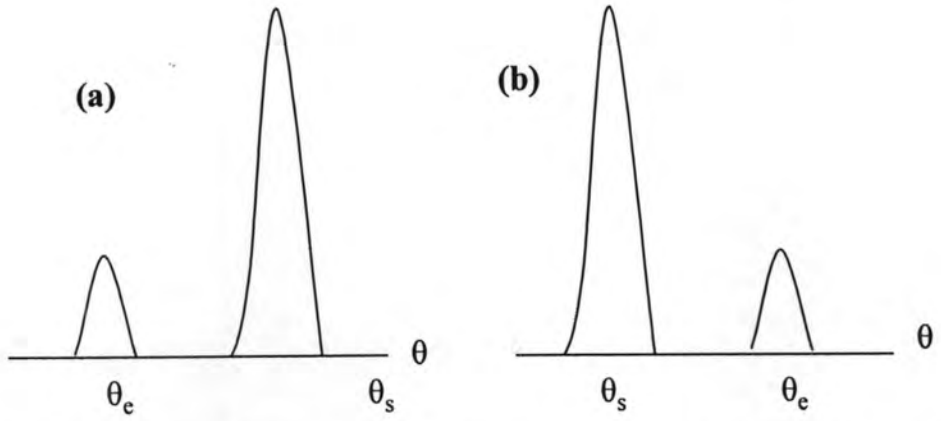

Figure 3.11 diffraction peaks from the epitaxial layer (at θ_e) and the substrate (at θ_s) under a (a) compressive strain and (b) tensile strain.

In the strained epitaxial growth, the lattice constants of the strained film in the direction parallel and perpendicular to the interface are

$$a_{//} = \frac{a_l d_1 + a_s d_0}{d_1 + d_0} \tag{3.16}$$

$$a_{\perp} = (1 - \sigma\varepsilon) a_l \tag{3.17}$$

where d_1, d_0 are film thicknesses and substrate and σ is a Poisson ratio which is given by

$$\sigma = \frac{C_{11}}{2C_{12}} \tag{3.18}$$

where C_{11} and C_{12} are elastic constants of the epitaxial layer. The C_{11} and C_{12} for InAs are 8.329×10^{11} and 4.526×10^{11} dyn/cm^2 and for GaAs are 11.88×10^{11} and 5.38×10^{11} dyn/cm^2 respectively.

To calculate the alloy composition from the lattice constant, its dependence on the composition must be determined. In the case of fully relaxed layers, the $a_{\perp}$ can be measured by using Vegard's law. However, Vegard's law is no longer true for strained layer. In this case, both lattice parameters ($a_{\perp}$ and $a_{//}$) are considered to determine the alloy composition. The In concentration from the $In_xGa_{1-x}As$ alloy layers can easily be determined from the free lattice constant (a_{InGaAs}) using Vegard's law which can be expressed by the following formulae:

$$a_{InGaAs} = \frac{2C_{12}a_{//} + C_{11}a_{\perp}}{2C_{12} + C_{11}} \tag{3.19}$$

$$a_{InGaAs} = x a_{InAs} + (1-x) a_{GaAs} \tag{3.20}$$

$$C_{11} = \frac{x a_{InAs} C_{11}^{InAs} + (1-x) a_{GaAs} C_{11}^{GaAs}}{a_{InGaAs}} \tag{3.21}$$

$$C_{12} = \frac{x a_{InAs} C_{12}^{InAs} + (1-x) a_{GaAs} C_{12}^{GaAs}}{a_{InGaAs}} \tag{3.22}$$

The important concept in strained epitaxial layer is critical thickness. Critical thickness arises because of a competition between strain energy and chemical energy. Below the critical thickness, minimum energy state of the bilayer system is achieved

by strain. Above the critical thickness, the minimum energy state is achieved by the formation of dislocations (Bhattacharya, 1994).

If the coherent strain becomes relatively large either due to a large lattice mismatch or a large thickness of the epitaxial layer, the strain energy is reduced by the formation of dislocation at the interface which is given by (Bhattacharya, 1994)

$$E_{St} = f^2(C_{11} + C_{12} - \frac{2C_{12}^2}{C_{12}})d_1 \tag{3.23}$$

The critical thickness as a function of strain is given by (Fritz et al., 1985)

$$\varepsilon = \frac{a_s}{\sqrt{2}h_c}\frac{(1-\sigma/4)}{2\pi(1+\sigma)}(\ln\frac{\sqrt{2}h_c}{a_s}+1) \tag{3.24}$$

where ε is the strain, h_c is the critical layer thickness, a_s is the lattice constant of the substrate and σ is Poisson ratio. The theoretical graph of critical thickness derived from equation (3.24) as a function of strain for $In_xGa_{1-x}As/GaAs$ is shown in Fig. 3.12. This form of Matthews-Blakslee formula is obtained from the equation 5 of Ref paper (Matthews and Blakslee, 1974) by substituting $f=2\varepsilon, b = a/\sqrt{2}$, cosα = cosλ = 1/2 which are appropriate for the InGaAs/GaAs system.

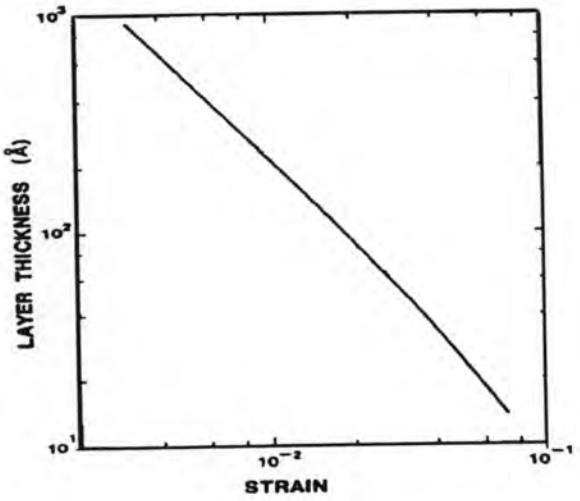

Figure 3.12 Theoretical graph for critical thickness of InGaAs as a function of strain (Fritz et al., 1985).

From this figure, the h_c depends on the amount of lattice mismatch (strain) of particular material. The h_c decreases with the strain increases. This result provides information for design of strained-layer devices.

3.3.2 Defects

In semiconductors, the reasons of introduction to defects are either thermodynamic considerations or the presence of impurities during the crystal growth process. Therefore, the regular pattern of atomic arrangement in crystal is interrupted by defects. Four types of defects in crystalline semiconductors are generally characterized as (i) point defects, (ii) line defects, (iii) planar defects and (iv) volume defects.

3.3.2.1 Point Defects

A point defect is a highly localized defect that affects the periodicity of the crystal only in one or few unit cells (Singh, 2003). The common defects which usually occur in binary GaAs compound is anti-site defect in which one of the atoms from Ga atom sits on the As sublattice instead of the Ga sublattice. Other point defect is interstitial defect where an atom sits in a site that is in between the lattice points. A schematic showing some important point defects in a crystal is shown in Fig. 3.13.

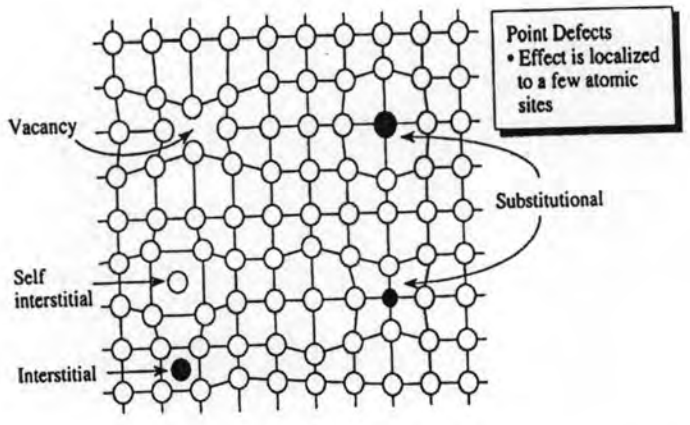

Fig. 3.13 Schematic diagram showing point defects in a crystal (Singh, 2003).

3.3.2.2 Line Defects or Dislocations

When the large number of atomic sites is misaligned, the resulting defect is called a line defect or dislocation. There are two major types of dislocations, namely,

edge dislocation and screw dislocation. When an extra half plane of atoms is inserted to a perfect crystal, a defect known as an edge dislocation is created in the regular atomic structure along the line where the extra half-plane terminates as shown in Fig. 3.14(a). A screw dislocation shown in Fig. 3.14(b) can be visualized as being formed by cutting the crystal pathway through with a knife and shearing it parallel to the edge of the cut by one atom spacing. The screw dislocation transforms successive atom planes into a helix around the dislocation line. The characteristic of both edge and screw dislocations is termed as mixed dislocation as shown in Fig. 3.15 (Andrew et al., 2002). The dislocations present in real crystalline solid are commonly of mixed dislocation. Dislocations are generally described by the Burgers vectors and the dislocation line. From Fig. 3.15(a), relaxation occurs via threading dislocation (TD) motion and MD formation on the inclined glide planes. The most common slip system is a/2(110) {111}. The Burgers vectors for this system are along the face diagonals of the cubic cell and are the shortest possible primitive lattice translation vectors. The set of possible Burgers vectors can be constructed by considering the edges of a half octahedron, as shown in Fig. 3.15(b). The dislocation Burgers vector can be decomposed into edge b_{edge} and screw b_{screw} components. Consequently, the edge component can be decomposed into parts parallel $b_{//}$ and perpendicular $b_{\perp}$ to the film/substrate interface: $b_{edge}=b_{//}+b_{\perp}$.

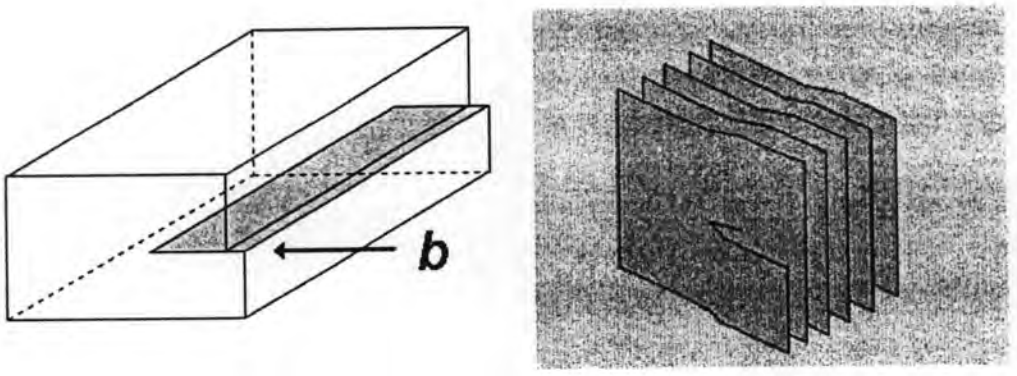

Figure 3.14 Schematic representation of (a) edge dislocation and (b) screw dislocation (http://en.wikipedia.org/wiki/Dislocation#Edge_dislocations).

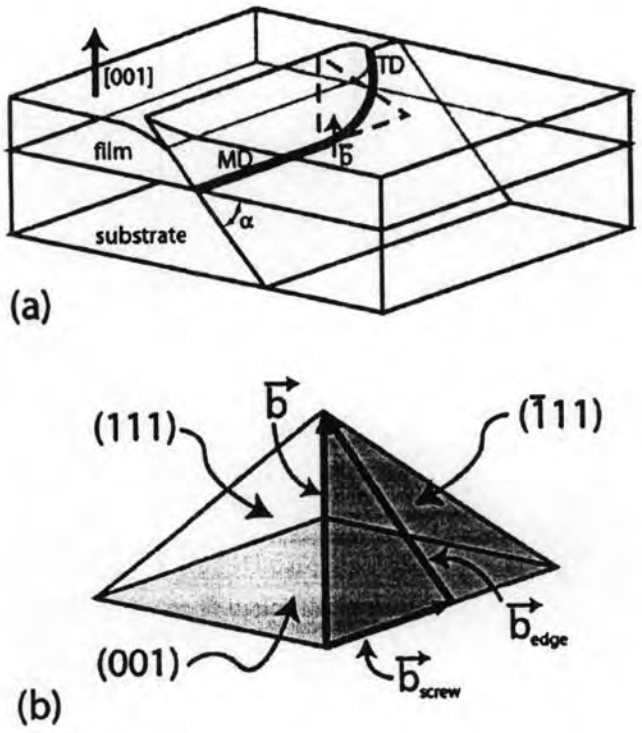

Figure 3.15 Dislocation geometry in heteroepitaxial mismatched thin films. (a) One of the inclined {111} planes for a (001) oriented fcc film/substrate system with a gliding TD segment and a trailing MD. (b) Dislocation Burgers (Andrew et al., 2002).

In order to get a better understanding of dislocation with Burgers vector, the basic information about Burgers vector is explained. A dislocation is given in terms of the Burgers circuit. A Burgers circuit is any atom to atom path taken in a crystal containing dislocations which forms a closed loop. The vector required to complete the circuit is called the Burgers vector. Therefore, the orientation and magnitude of a dislocation can be characterized in terms of its Burgers vector. The Burgers vector of edge dislocation is perpendicular and screw dislocation is parallel to the line of the dislocation. The schematic diagram for Burgers circuit and Burgers vector is illustrated in Fig. 3.16. In general case, the dislocation line lies at an arbitrary angle to its Burgers vector. However, the Burgers vector of the dislocation is always the same and independent of the position of the dislocation. There are two basic types of dislocation movement. They are (i) glide or conservative motion and (ii) climb or non-conservative motion. In glide motion, the dislocation *moves in* the surface defined

by its line and Burgers vector. In climb motion, the dislocation *moves out* of the glide surface.

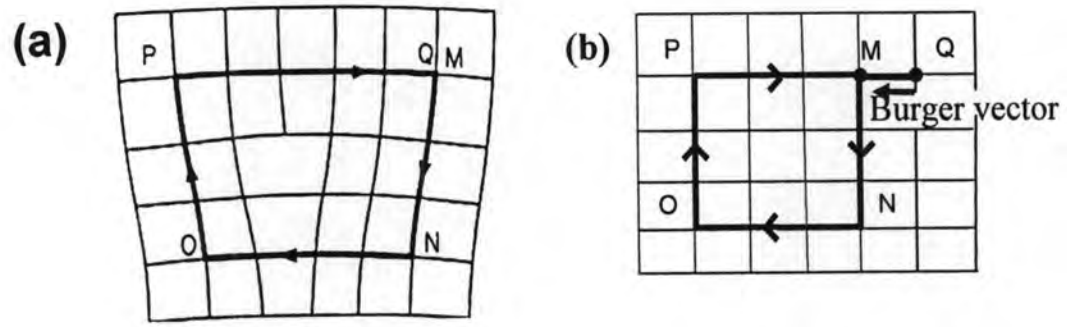

Figure 3.16 Burgers circuit (a) around a dislocation and (b) in a perfect crystal (Hull, 1965).

3.3.2.3 Planar and Volume Defects (Sigh, 2003)

Planar and volume defects are not important in single crystalline materials, but can be importance in polycrystalline materials. If the Si is grown on glass substrate, small regions of Si are perfectly crystalline but are next to microcrystallities with different orientations. The interface between these microcrystallities is called grain boundries. Grain boundaries may be viewed as array of dislocations.

Volume defects are introduced if the crystal growth process is poor. The crystal may contain regions that are amorphous or may contain voids. In most epitaxial growth techniques used in modern optoelectronics, these defects are not a problem. However, the development of new material systems such as diamond (C) or SiC are hampered by such defects.

3.3.3 Dislocations

There are many models for the generations of MDs. MDs are associated with TDs and extend into a film growing epitaxially on the substrate. The formation of MDs for the strained layer heterostructures for various lattice-mismatched systems are shown by both qualitatively (Shiryaev, et al., 1997; Liu et al., 1999; Samonji, et al., 1999; Takano et al., 2005) and quantitatively (Andrew, et al., 2002; Hoagland, et al., 2004).

3.3.3.1 Critical thickness for $In_xGa_{1-x}As$ Growth on GaAs

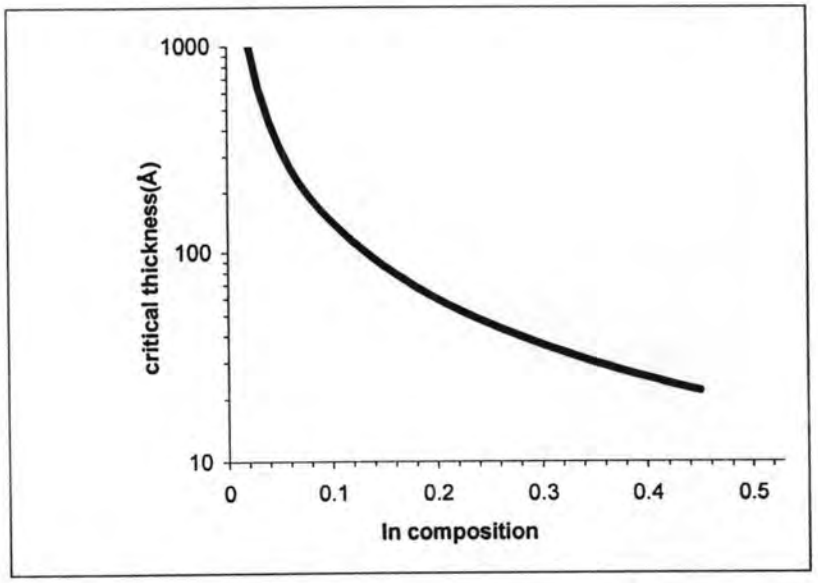

Figure 3.17 Critical thickness for defect introduction for $In_xGa_{1-x}As$ on GaAs.

The critical thickness for MDs via glide of threading dislocations for both a single strained layer and multilayered has been explored by many authors (Matthews et al., 1974; Freund, 1990; Hirth at al., 1990). The critical thickness from Matthews and Blakslee's model is the thickness at which MDs are formed. However, the critical thickness determined from the change in Bragg peak separation from XRD measurement is the thickness at which the strain is already relieved by at least 10^{-4}. Therefore, strain relief at h=hc given by Matthews and Blakslee's model is much less than 10^{-4}. For the relaxation of a single strained InGaAs layer on GaAs substrate via the introduction of MD, h_c of the strained layer is given by (Wie, 1993)

$$h_c=A|x-x_0|^{-b} \qquad (3.23)$$

where A= thickness of the film (8.16Å)

b= strength of dislocation (1.24),

x= In composition ($0<x<0.4$), and

$x_0=0$

The parameters are from the equilibrium theory of Matthews and Blakeslee (1974). According to the theory, the critical thickness is the thickness at which the MDs are just formed at the substrate/epilayer interface through glide of pre-existed

threading dislocation (TD) in the substrate. The theoretical plot of the critical epilayer thickness of $In_xGa_{1-x}As$ on GaAs (001) as a function of the concentration of indium is shown in Fig. 3.17.

3.3.3.2 Types of Misfit Dislocations

There are two types of MDs in (001) epitaxial zinc-blende crystals or diamond cubic systems for low lattice mismatched (001) interfaces. They are α type and β type dislocations that are classified according to the termination of dislocation core. The dislocation line along the [1-10] direction with As atoms at the core are defined as α type dislocation. On the other hand, the dislocation lines along [110] direction with Ga atoms at the core are known as β type dislocation (Wu et al., 1999).

Many research groups have investigated asymmetries of dislocation lines. Abrahams et al. (1969) suggested that the occurrence of such an asymmetries effects are due to differences in the nucleation or mobility of these two types of dislocations (Abrahams et al, 1969). Kuesters et al. (1986) reported that the velocity of α type dislocation is much greater than that of β type dislocation under the investigation with TEM results. Kavanagh et al. (1988) investigated the dislocation densities, surface morphology and strain of GaInAs/GaAs epitaxial interfaces as a function of indium composition and layer thickness by TEM, medium energy ion-blocking measurement and double-crystal x-ray diffractometry. They claimed that asymmetries in dislocation densities are due to unequal distribution of Burgers vector of 60° type or edge type dislocation densities in the strained layer which in turn responsible for the strain asymmetry in strained layer (Kavanagh et al., 1988). Many experimental results additionally confirm that the argument of asymmetry in MDs along <110> direction. Anisotropic strains in InGaAs/GaAs layer along [1-10] direction are much larger than along [110] direction (Hiwatashi et al., 1998; Samonji et al., 1999; Zhang et al., 2006). Alternative results of anisotropy strain are shown by other reports. They reported that anisotropic strains along [110] directions are larger than along [1-10] directions (Beanland et al., 1995; Kavangh et al., 1988; Kim et al., 2004).

3.3.3.3 Surface Steps via Threading Dislocation

Hongland et al. (2004) reported influence of surface steps on glide of TDs during layer growth. They demonstrated the surface step via the glide of TD, which is energetically favorable when the thickness of the layer exceeds a critical value, is shown in Fig. 3.18. This group quantitatively proved that critical values for MDs are larger than predicted by traditional stepless solution from the energy point of view required to form a unit length of dislocation with edge and screw Burgers vector components, b_e and b_s respectively on the interface.

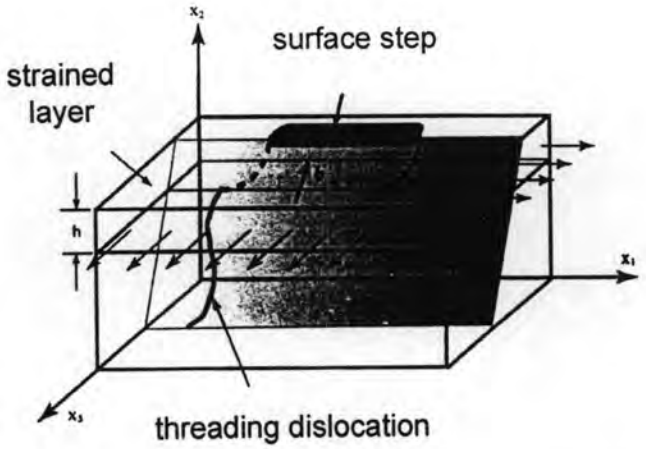

Figure 3.18 Geometric of appearance of surface step via gliding of threading dislocation with Burgers vector b (Hongland et al., 2004).

The TDs elongate to form MD segments during the growth of GaAs/In_xGa_{1-x}As/GaAs under the investigation by TEM measurement are shown in Fig. 3.19 (Liu et al., 1999). The surface steps are seen as 2D arrays so-called cross hatch when we look at from the top as seen in plan view of AFM and TEM images in Fig. 3.20 (a) and (b) (Yastrubchak et al., 2003). Since the Burgers vector makes an angle of 60° to the line direction, this type of MD is commonly called a 60° dislocation. One of the primary features of the dislocation structure is V-type configuration emerging from the interface between the substrate and strained layer into the surface buffer layer in InGaAs/GaAs strained layer superlattices structure (Rajan et al., 1987). The apex angle of the V-shape is ~70°. They claimed that the formation of V-shape is due to

annihilation of inclined MDs segments of expanding slip loops originating in the MD network. TEM image of V-shape configuration is shown in Fig. 3.21.

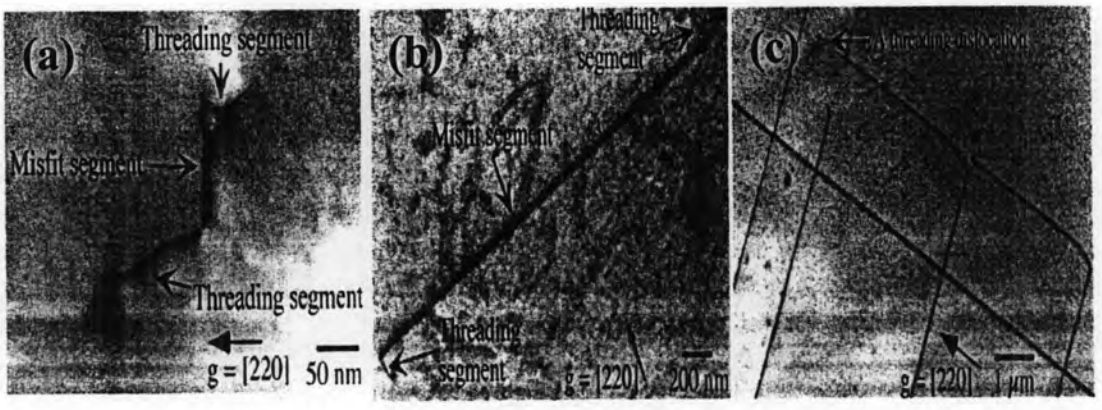

Figure 3.19 TEM images showing dislocation observed in GaAs/$In_{0.15}Ga_{0.85}As$/GaAs for various thicknesses (h) of InGaAs layers (a) misfit dislocation segment (h=6 nm) (b) elongated misfit dislocation segment (15 nm) and (c) misfit dislocation network with threading dislocation (h=25 nm) (Liu et al., 1999).

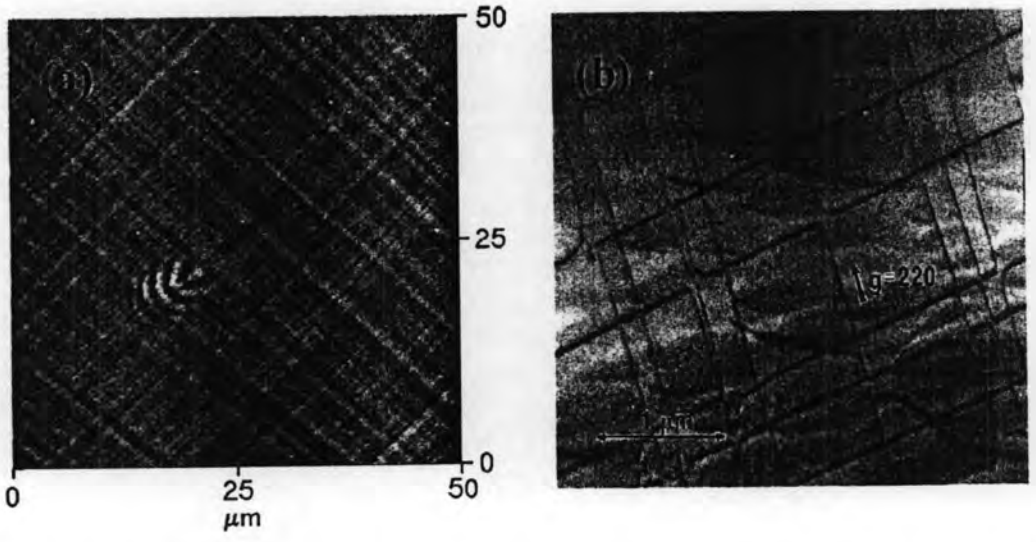

Figure 3.20 (a) AFM and (b) TEM images of cross-hatch pattern for $In_{0.25}Ga_{0.75}As$/GaAs (001) (Yastrubchak et al., 2003).

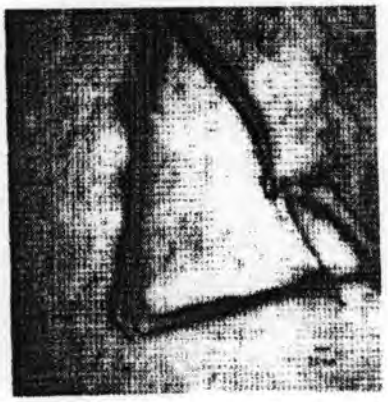

Figure 3.21 TEM image showing V-shape configuration resulted from inclined slip loops originating in misfit dislocation network (Rajan et al., 1987).

3.3.3.4 Lomer Type Misfit Dislocation

In heteroepitaxial growth, pure edge (Lomer type) misfit dislocations (L-MDs) are the most efficient at misfit strain. Pure edge MDs have been obtained on many heteroepitaxial systems such as SiGe/Si, Ge/GaAs, GaAlAsP/GaAs, GaAlAsSb/GaSb and InGaAsP/InP with (001)-oriented substrates (Vdovin et al., 1996); {111} (Ernst et al., 1993); {112} (Mitchell at al., 1991) substrate orientations. The number of L-MD fraction in the MD network depends on the lattice mismatch, growth thickness, epitaxial layer composition and the temperature or annealing (Hull and Bean 1989; Hull et al., 1989).

In the paper of Vdovin et al. (1997), two typical types so-called A type and B type in L-MDs of pure edge MDs characterized by different geometrical properties have been observed for different epitaxial systems. A type L-MDs are in a form of curved lines leaving the interface and greatly deforming the MD network. After that, they are generated via interaction of the parallel 60°-MDs pre-existing at the interface. B type L-MDs are long and difficult to identify generation mechanism which are frequently observed in the MD networks with low MD linear density. Both types are determined by the growth conditions and the mobility of individual dislocations in the film. The common dislocation node for initial 60°-MDs, arising as a result of the dislocation reactions in crossing points of the MDs, is a starting point for generation of the pure edge MDs. MD propagation is accompanied by a shift of dislocations from the interface upwards into the epilayer or downwards into the substrate. The

schematic configuration for the generation L-MD of pure edge MD is shown in Fig. 3.22 (Vdovin, 1997).

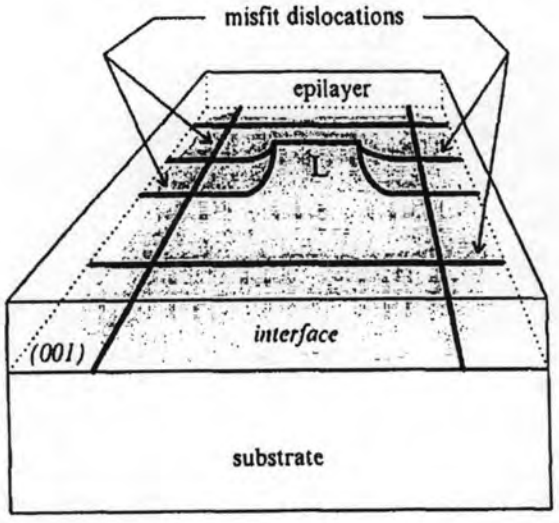

Figure 3.22 Schematic drawing of the spatial dislocation configuration for the case of L-MD which is commonly found in pure edge MD (Vdovin, 1997).

3.4 Ordered Quantum Dot Growth Techniques

This part surveys various alternative growth techniques for ordered quantum dots which is the most important part in this chapter. Attempts to achieve alignment of self-organized QDs are compiled for different material systems such as Ge/Si, InGaAs/GaAs and InP/GaAs. Various attempts have been performed towards improving site control for self-organized QDs, which is of importance for fabrication of devices. The basic concepts of QDs growth introduced are based on two growth approaches. First approach is QDs are grown with various templates and the second one is QDs are grown on different growth techniques. Since, the main work of this research is about the uniform QDs on the cross-hatch surface, nucleation of ordered QDs techniques is thoroughly reviewed in this part.

3.4.1 Growth on Templates

The growth of ordered QDs on various templates including high index substrate (Nishi et al., 1997; Wang et al., 2005), undulations (Häusler et al., 1996; Xie et al.,

1997; Hiwatashi et al., 1997; Kim et al., 2004; Zhang et al., 2006), corrugated (Mui et al., 1995; Jeppesen et al., 1996; Seifert et al., 1996b; Tusi et al., 1997; Konkar et al., 1998) or mask surfaces (Kamins et al., 1997) and superlattice templates(Wang et al., 2004; Mano et al., 2004) are presented in this section.

3.4.1.1 High Index Substrate Template

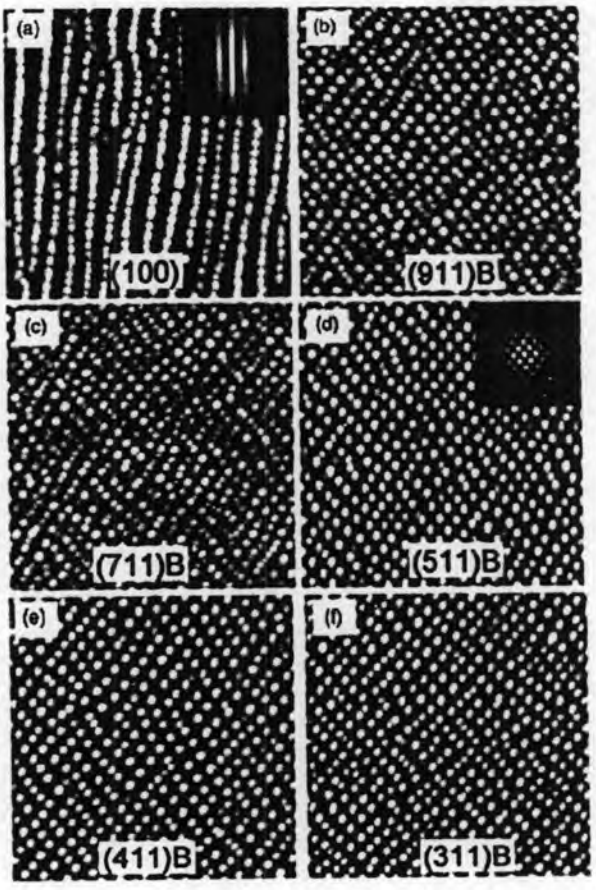

Figure 3.23 AFM images of (2 μm×2 μm) of the QD layers grown on (a) GaAs (100), (b) GaAs (911)B, (c) GaAs (711)B, (d) GaAs (511)B, (e) GaAs(411)B and (f) GaAs (311)B (Wang et al., 2005).

All parameters governing quantum dot formation depend on substrate orientation. QDs formation on high index substrates (n11) is different from formation on (001) substrates. Formation of $In_{0.3}Ga_{0.7}As$ dots on (311)B substrates during hydrogen assisted MBE was reported by Chun et al. (1996). Nishi et al. (1997) have also grown ordered islands by gas source MBE. A typical base diameter of the dot is

about 120 nm. The height varied from 3 to 13 nm for an increase in the nominal thickness of the $In_{0.25}Ga_{0.75}As$ layer from 4 to 8 nm. Ordering of islands along lines inclined about 60° from [110] direction is observed. Wang et al. (2005) claimed that 1D and 2D laterally- ordered multilayered arrays of InGaAs QDs are grown on GaAs (001) and GaAs (n11)B (where n is 3, 4, 5, 7 and 9). The optimum substrate was found (511)B GaAs which is deduced from different PL linewidths among samples on various substrates. The narrowest PL linewidth of 23 meV is observed from the QDs grown on GaAs (511) B substrate. Remarkably, the ordered pattern can be adjusted by selecting different high index substrates. 1D ordering arrays of QDs can be achieved only on GaAs (001) while 2D ordering of QDs can be observed on GaAs high index substrates shown in Fig. 3.23.

3.4.1.2 Undulations Template

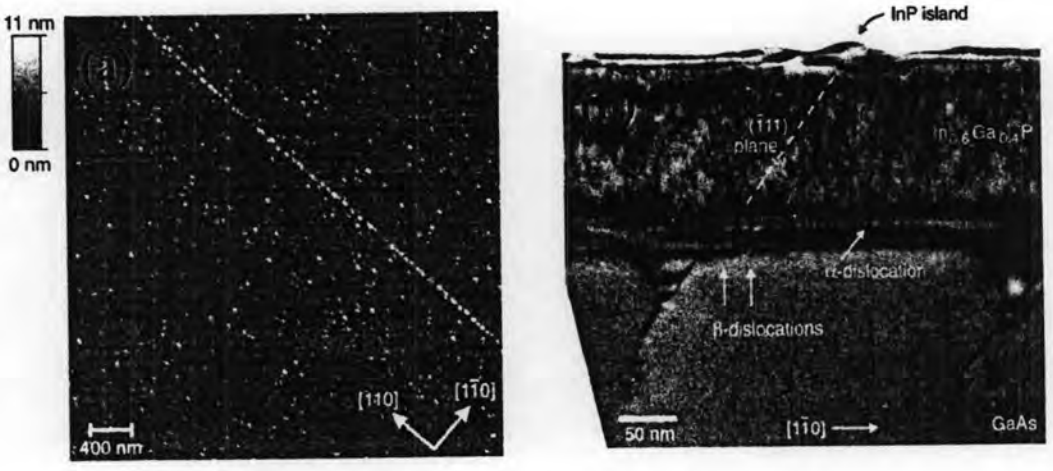

Figure 3.24 (a) AFM and (b) cross-sectional TEM images of a 15 ML of InP QDs grown on 150-nm thick $In_{0.61}Ga_{0.39}P$ layer (Häusler et al., 1996).

Alignment of InP dots along <110> on the MDs created in a $In_{0.61}Ga_{0.39}P$ buffer on GaAs (001) grown by MBE was reported by Häusler et al. (1996). QDs are found on the top of the surface ridges along the <110> direction as seen in Fig. 3.24(a). The size of the individual InP QDs varies between 20 to 30 nm in diameter and 5 to 10 nm in height. A pronounced alignment over a distance of more than 4 μm is observed along [110] direction. V-shape tips in Fig. 3.24(b) extending deeply into the substrate

are clearly seen as we have already shown in Fig. 3.21. InP QDs are preferentially nucleated on the top of the surface undulation and most of the islands are slightly elongated along [110] direction where the degree of strain is the highest.

Ge dots are found to nucleate on the intersection of [110] and [1-10] MDs shown in Fig. 3.25(b) (Xie et al., 1997). Schematic drawing of a relaxed template of SiGe based on a Si(100) substrate is shown in Fig. 3.25(a). The dislocation network is formed at the interface of the Si substrate and SiGe buffer layer. Ge dots are deposited on top of a thin Si capping layer. The average dislocation distance is 100 nm, but dislocation spacing varies randomly. The typical Ge dot size is 200 nm. The spacing of rows and columns decorated with Ge dots is about 1 μm, much larger than the average dislocation distance, and corresponds to groups of dislocations that are closely spaced.

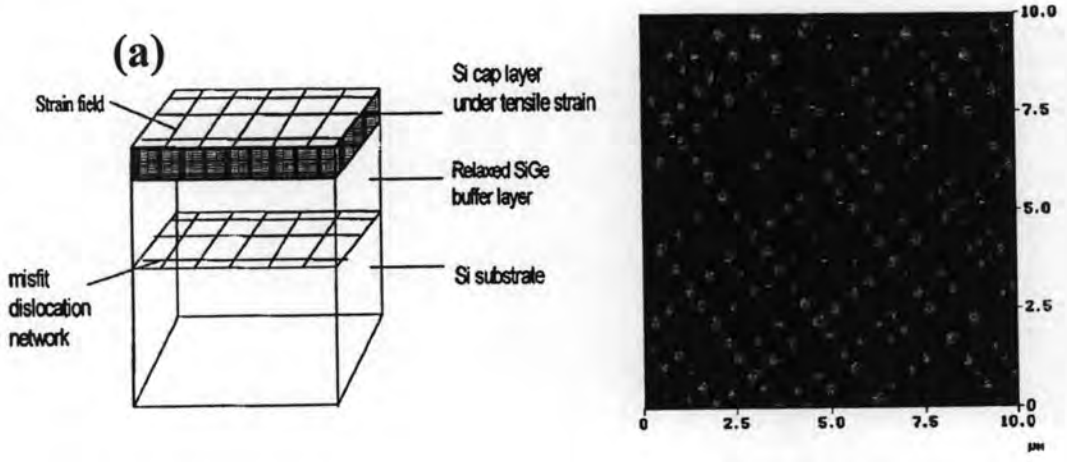

Figure 3.25 (a) schematic display of a relaxed template of SiGe based on a Si (100) substrate and (b) AFM image (10 μm×10 μm) of Ge islands on the Si layer above a misfit dislocation network (Xie et al., 1997).

Hiwatachi et al. (1997) proposed aligned QDs on the undulating surface by varying the different thicknesses (43~1200 nm) of $In_xGa_{1-x}As$ (x=0.07~0.21) layers. InAs QDs are found on the strain distributed InGaAs surfaces along the [110] and [1-10] crystallographic directions. At first, the residual strain on the InGaAs surface from the relaxation coefficient as a function of the various thicknesses of InGaAs layers is deduced. They found that strained InGaAs layer is relaxed more by the generation of MD at the InGaAs/GaAs heterosurfaces as the thickness of InGaAs layers increases. This means that percentage of relaxation coefficient increases as the thickness strained

InGaAs layers increases. While QDs along [1-10] directions are found only on the top of undulating surface, QDs along [110] directions are found both on the top and bottom of the corrugation surface shown in Fig. 3.26.

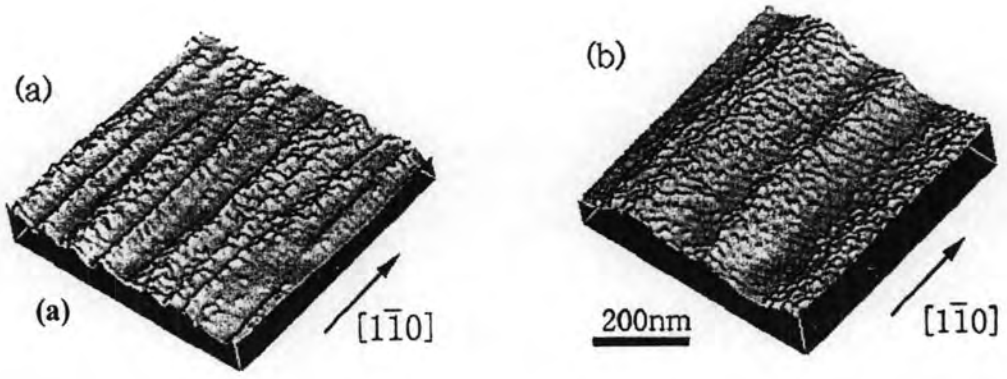

Figure 3.26 Images of InAs QDs on (a) 162 nm and (b) 325 nm of $In_{0.15}Ga_{0.85}As$ layers (Hiwatachi et al., 1997).

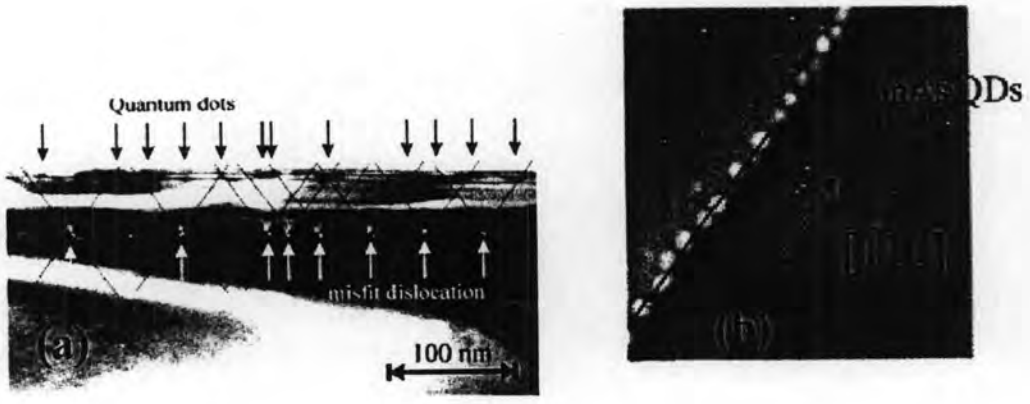

Figure 3.27 (a) A cross-sectional TEM image showing vertically 3 stacked InAs QDs on a strained layer with number of superlattice cycles (n) is 25 and misfit dislocations and (b) 0.5×0.5 μm^2AFM image of 1.6 ML of InAs QDs arrays grown on strain-engineered superlattice template with n is 30 (Kim et al., 2004).

By the formation of strain-engineered superlattice (SL) template consisting of 1 InAs ML/4 GaAs ML SL followed by 20 ML thick-GaAs spacer layer, Kim et al.

(2004) successfully obtained aligned InAs QDs on a SL along <110> direction (Kim et al., 2004). The number of SL cycles (n) was varied from 15 to 30. Then, a single-layer QDs and 3 stacked QDs having 20 ML GaAs barrier were grown for the formation of QDs. From the TEM image, 60° MD along <110> direction due to the partial excessive strain relaxation of SL were generated and gave rise to the selective formation of QDs along the ridges where strain energy is lower than that of other regions shown in Fig 3.27(a). The average width and height of QDs were 32.3 and 3.04 nm, respectively according to line depth profile taken from AFM image shown in Fig. 3.27(b).

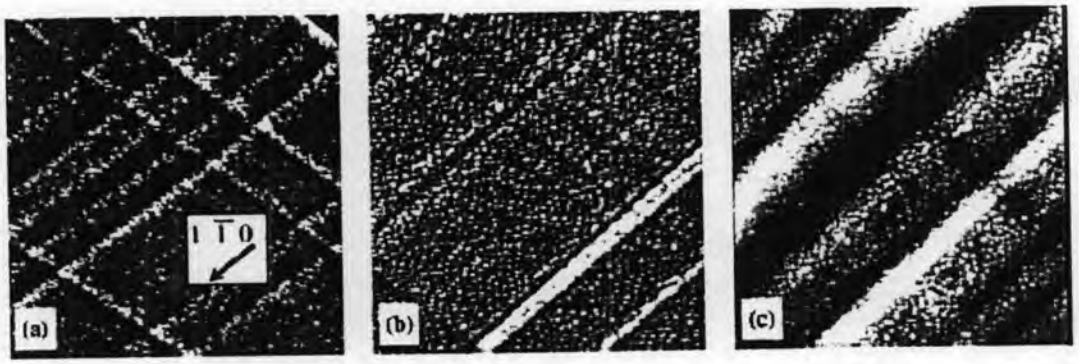

Figure 3.28 AFM images of (a) 0.8 ML, (b) 2 ML of InAs QDs on 50-nm $In_{0.15}Ga_{0.85}As$ layer and (c) 2 ML of InAs QDs on 180-nm $In_{0.15}Ga_{0.85}As$ layer (Zhang et al., 2006).

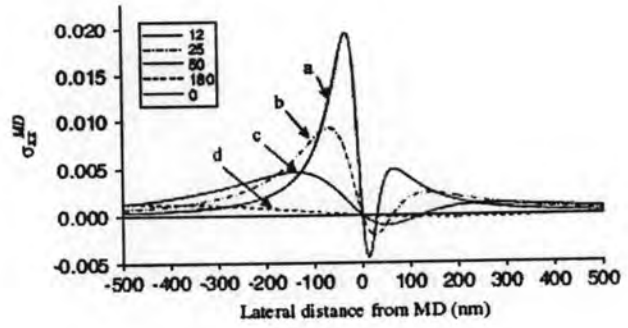

Figure 3.29 Graph of surface stress as a function of lateral distance from misfit dislocation (σ_{xx}) showing the reason of the ordering of QDs is weak when the InGaAs layer is relatively thick (Zhang et al., 2006).

Zhang et al. (2006) reported the InAs QDs grown on cross-hatch patterns and explained the influence of dislocation stress field on distribution of QDs quantitatively. They found that the cross-hatch grid is narrow when the $In_{0.15}Ga_{0.85}As$ strained layer is relatively thin (50 nm) and becomes asymmetric ridges and valleys. However, the ridges are wider and tend to be near symmetrical as the strained layer is relatively thick (180 nm) and the distribution of QDs on thick layer of InGaAs is also random in fashion. It means that the ordering of QDs is weak. Figure 3.28 shows AFM image and Fig 3.29 shows the graph of residual surface stress as a function of different lateral distance MD for different thicknesses of $In_{0.15}Ga_{0.85}As$ layers.

3.4.1.3 Corrugated or Mask Surfaces Template

On corrugated substrates, islands tend to nucleate at characteristic sites of the structure such as edges, side walls or trenches. Mui et al. (1995) reported the alignment of InAs islands grown using MBE along ridges that have been fabricated using wet chemical etching. Rather large pitch (1 μm) islands are found to nucleate on the side walls for ridges along [011] as shown in Fig. 3.30(a) and are found on the (001) top of the mesas or at the foot of the mesas for ridges along [01-1] as shown in Fig. 3.30(b). On short (0.28 μm) pitch, V-grooves islands are only found at the bottom and the side wall of the grooves as shown in Fig. 3.31. The typical size of island is 40 nm in diameter and 12 nm in height.

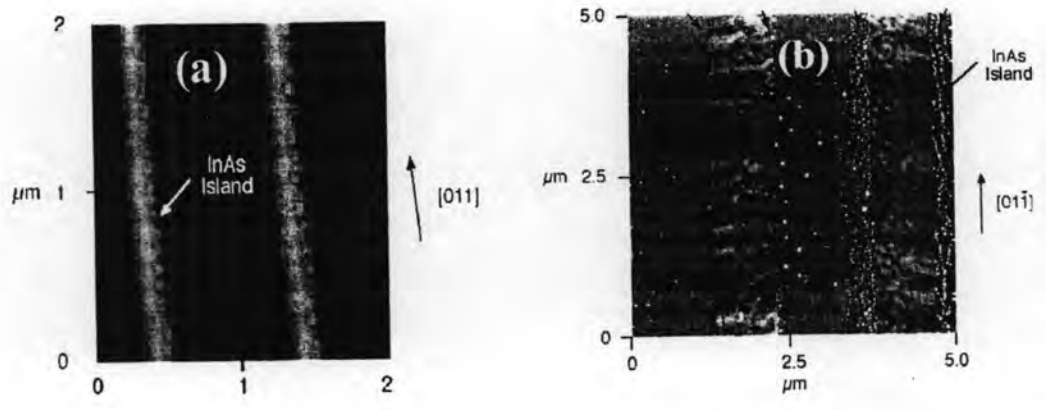

Figure 3.30 AFM images of InAs QDs aligned along the (a) [011] and (b) [01-1] oriented ridges (Mui et al., 1995).

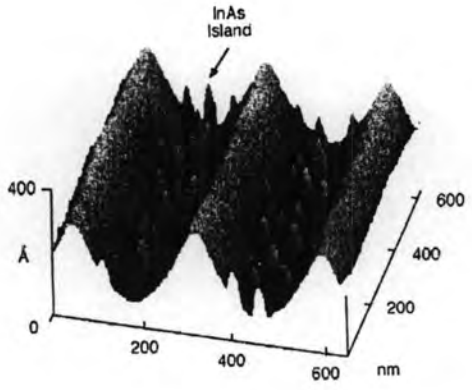

Figure 3.31 AFM image of V-grooves InAs islands aligned along [01-1] oriented ridges (Mui et al., 1995).

Kamins et al. (1997) reported the location of Ge islands on top of Si (001) ridges with {110} side walls grown on stripe-like openings in an SiO_2 mask (Fig. 3.32 b). For fairly wide ridges (670 nm up to 1.7 μm) several rows of Ge islands are formed on the mesa top along the edges. On narrow ridges (450 nm) one row of Ge islands is found to sit along each edge (Fig. 3.32 a). In these two rows, having a distance of 300 nm, the Ge islands are almost perfectly periodic with an average distance of about 85 nm.

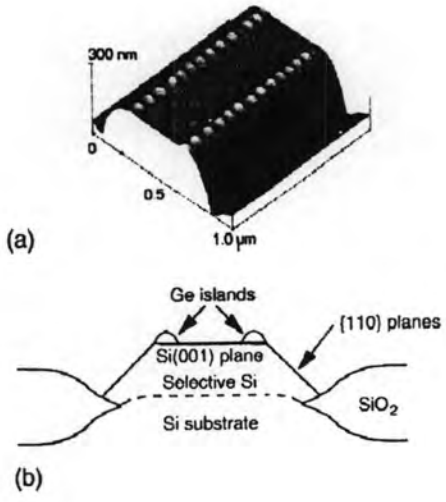

Figure 3.32 (a) Three dimensional display of an AFM image of a 450 nm wide Si ridge along <100>. Ge islands line up along the edges of the mesa. (b) The corresponding cross-sectional of schematic (Kamins et al., 1997).

3.4.1.4 Superlattice Template

Recently, Wang et al. (2004) investigated the growth of multilayered (In,Ga)As QDs separated by GaAs (001) substrate. The effect of GaAs capping and (In,Ga)As coverage on the formation of QD chains is investigated. It is found that by introducing GI time (10 sec) during the initial stages of the growth of the 3 ML of GaAs spacer layer, the QD chains are lengthened to over 5 μm along the [01-1] direction. Moreover, this group shows that the QD alignment in the (In,Ga)As QD chains is very sensitive to ML coverage. The longest QD chains can be obtained when the deposition coverage is 6 ML. The AFM images showing long chain of QDs with different ML thicknesses are shown in Fig. 3.33.

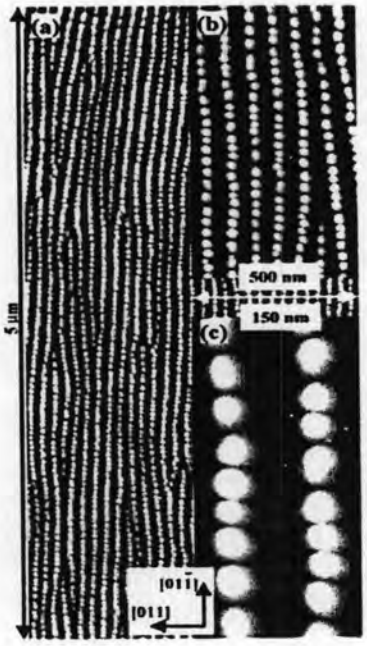

Figure 3.33 AFM images of (a) 6 ML in different scales and (b) and (c) are shown in different scales of $In_{0.5}Ga_{0.5}As$ QD multilayers (Wang et al., 2004).

The growth technique of Wang group is modified by Mano et al. (2004) by annealing the GaAs capping layer at higher temperature in order to further elongate QD chains. In their growth techniques, the main five steps of growth processes are as follows: (i) random formation of elongated (In,Ga)As QDs at elevated temperature on the GaAs buffer layer (ii) growth of a thin GaAs capping layer (iii) annealing at

higher temperature (iv) growth of the GaAs separation layer and (v) growth of the subsequent (In,Ga)As QD layer. By repeating these steps in (In,Ga)As/GaAs SL growth, 1D QD array is extended to over 10 μm length with a small number of branches shown in Fig. 3.34.

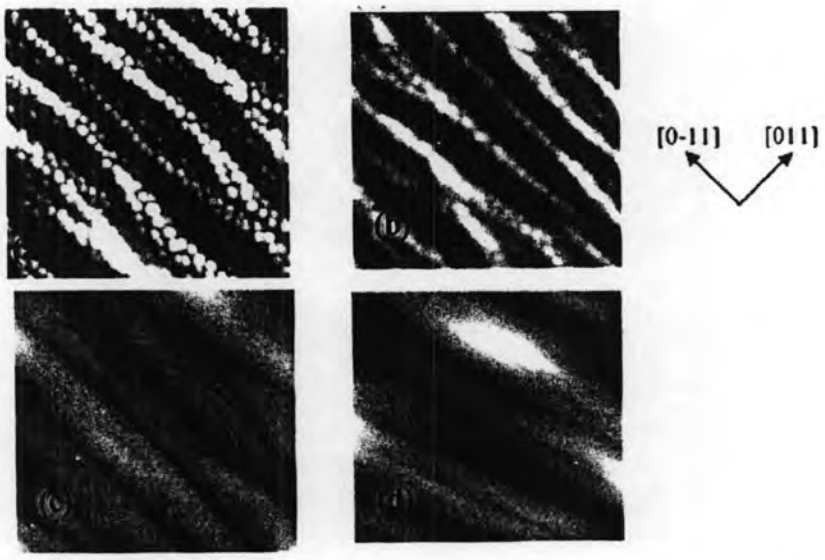

Figure 3.34 AFM images of the surfaces during formation of the sixteenth period of the (In,Ga)As 2.3nm/GaAs 13.0 nm QWR template (a) 2.3 nm $In_{0.41}Ga_{0.59}As$ grown at 540°C (b) 0.7 nm GaAs cap deposited at 540°C without growth interruption (c) annealing at 580°C for 2 min and (d) 12.3 nm GaAs grown at 580°C (Mano et al., 2004).

3.4.2 Growth Techniques

Many order QDs growth techniques are reviewed in this part such as multi step (Kitamura et al., 1995; Akiyama et al., 2006) In-interruption growth (Hong et al., 2006), thin-cap and regrowth (Suwaree et al., 2006) and atomic force tip-induced nano-oxidation, atomic-hydrogen etching/cleaning and regrowth techniques (Kim et al., 2006).

3.4.2.1 Multi Steps Technique

Kitamura et al. (1995) demonstrated that the alignment of QDs along surface steps for (001) GaAs substrates misoriented by 2° toward [010], [110], and [1-10] using multiatomic step structures in MOCVD growth. In this technique, first, GaAs epilayer with multi atomic steps structure is grown on a vicinal GaAs substrate under appropriate growth conditions. Then, InGaAs quantum dots are grown on a vicinal substrate. Figure 3.35 visualizes the alignment of InGaAs QDs with a diameter below 20 nm along multiatomic surface steps for the [010] misoriented surface.

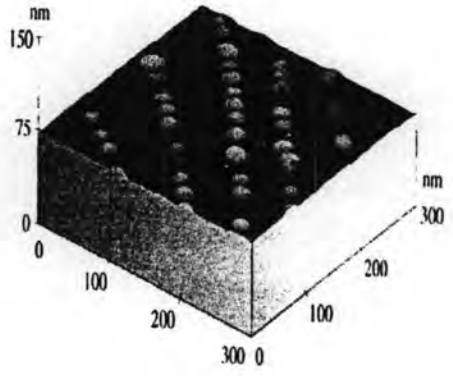

Figure 3.35 AFM image (300 nm×300 nm) of InGaAs QDs aligned multiatomic steps on GaAs (001) surface misoriented by 2° toward [101] direction (Kitamura et al., 1995).

InGaAs QDs arrays aligned on vicinal (111)B GaAs substrate tilted 8.5° towards the [-10-1] direction have been reported by Akiyama et al. (2006). First, SL buffer layer consisting of ten periods of 3 nm GaAs/ 10 nm AlGaAs are grown on the (111)B GaAs substrate. Then, when 50-nm-thick GaAs layer are deposited at a substrate temperature 600°C onto the SL buffer layer, a bunching of atomic steps called quasiperiodic corrugation of about 20 nm in period and about 2 nm in height are induced as shown in Fig. 3.36(a). It is worthy to note that they used low growth rate of GaAs, 0.05 nm/s and high As_4/Ga flux ratio is 500-700 in order to be effective in making the multiatomic steps quite straight and almost periodic.

The AFM image of InGaAs QDs grown by depositing the 3-nm-thick $In_{0.3}Ga_{0.7}As$ layer at T_s 520°C is shown in Fig. 3.36(b). Each train of island is aligned

along the [-101] direction, parallel to the underlying GaAs multiatomic steps. The array of island trains has the average period of about 50 nm, which is nearly twice as large as that of underlying GaAs multiatomic steps. The height of islands are 3-5 nm and lateral sizes are about 50-60 nm along the island trains. Neighboring islands are separated by small gaps of about 5-10 nm. The average density of islands is 3×10^{10} cm^{-2}.

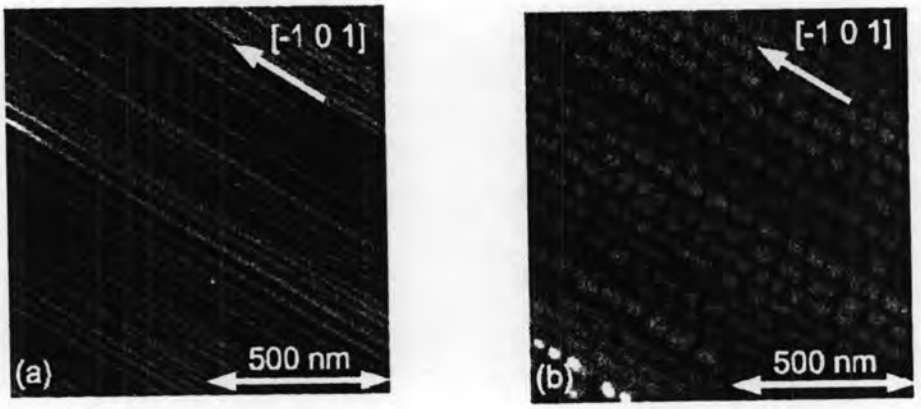

Figure 3.36 AFM image (a) of multiatomic steps on GaAs layer grown on a vicinal (111)B GaAs and (b) InGaAs islands by growing 3-nm-thick $In_{0.3}Ga_{0.7}As$ layer onto GaAs multiatomic sites (Akiyama et al., 2006).

3.4.2.2 In-Interruption Growth Technique

Ordered QDs on a more conventional GaAs (100) substrate using In-interruption growth technique shown in Fig. 3.37(a) are obtained without doing any complicated steps which was proposed by Hong et al. (2006). Indium atoms are interrupted while arsenic atoms supplying all the time during the growth of QDs. Therefore, In sources arriving at the substrate have a migration time to reach a more suitable site and this effect results in aligned QDs. AFM image of InAs QDs with 9 sec In-interruption time is shown in Fig. 3.37(b).

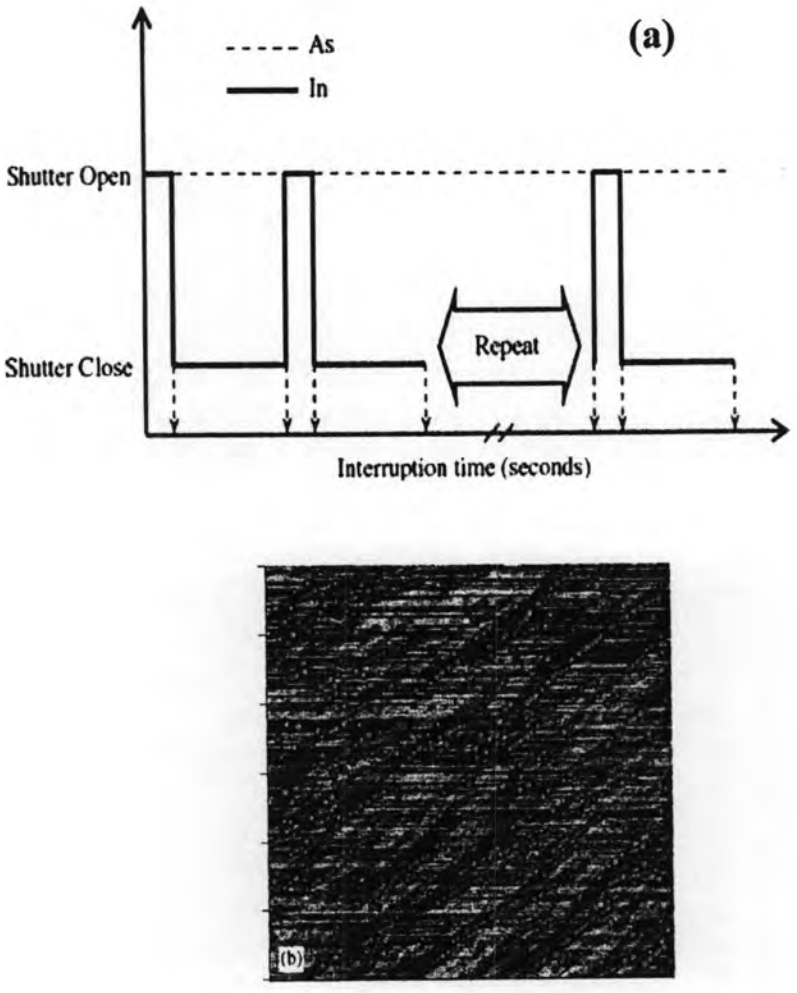

Figure 3.37 (a) Schematic drawing of In-interruption growth technique and (b) AFM image (3000 nm×3000 nm) of InAs QDs with a In-interruption time 9 sec (Hong et al., 2006).

3.4.2.3 Thin-Cap and Regrowth Technique

Recently, ordered InAs QDs grown on GaAs (001) substrate using a thin-capping-and-regrowth of QDs technique is demonstrated by Suwaree et al. (2006). By using a conventional QDs growth technique, as-grown randomly distributed QDs are formed on flat surface firstly. Then, on top of these QDs layers, thin GaAs layer (6ML) is capped. Because of the lattice mismatch between the QDs and capping layer, the strain energy around the QDs is increased. Correspondingly, In atoms migrate out from the QDs and leave a nanohole in the middle of the QDs. By

regrowing the QDs on top of nanoholes via a thin-capping process, nanopropeller QDs are formed. By repeating the thin-capping-and-regrowth process for 7 cycles at the regrown thickness of 0.6 ML, nanopropeller QDs are aligned along the [1-10] direction. AFM images of evolution of laterally aligned QDs along [110] are shown in Fig. 3.38.

Figure 3.38 AFM images of (a) nanohole (b) 1 cycle (c) 7 cycles of thin-cap and regrowth of QDs on nanoholes (Suwaree et al., 2006).

3.4.2.4 Atomic Force Tip-Induced Nano-Oxidation, Atomic-Hydrogen Etching/Cleaning and Regrowth Technique

Even more recently, the combination of atomic force microscope tip-induced nano-oxidation, atomic-hydrogen etching/cleaning and regrowth of InAs QDs by using droplet epitaxy technique is performed by Kim et al. (2006). A promising way to obtain site-controlled QDs with high quality based on the patterning and regrowth process, which can reduce the interface defects and contaminants between QDs and nanoholes to a negligible level, is suggested. Nano-oxide dots on GaAs surface are created by AFM tip-induced nano-oxidation in a contact mode. Then, these nano-oxide dots are removed by soft etching in order to form nanoholes. Finally, indium is supplied by droplet epitaxy method. The schematic illustration of the experimental procedures is shown in Fig. 3.39 and the AFM images of grown nanostructures by atomic force tip-induced nano-oxidation, atomic-hydrogen etching/cleaning and regrowth technique is shown in Fig. 3.40.

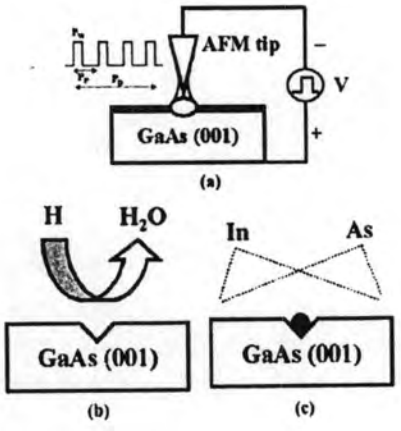

Figure 3.39 The schematic illustration of the experimental processes for (a) the formation of the nano-oxide dots on GaAs (001) surface by AFM tip-induced oxidation, (b) the subsequent removal of a nano-oxide dot and native oxide layer by atomic hydrogen irradiation and (c) the deposition of InAs QDs on nanoholes by droplet epitaxy.

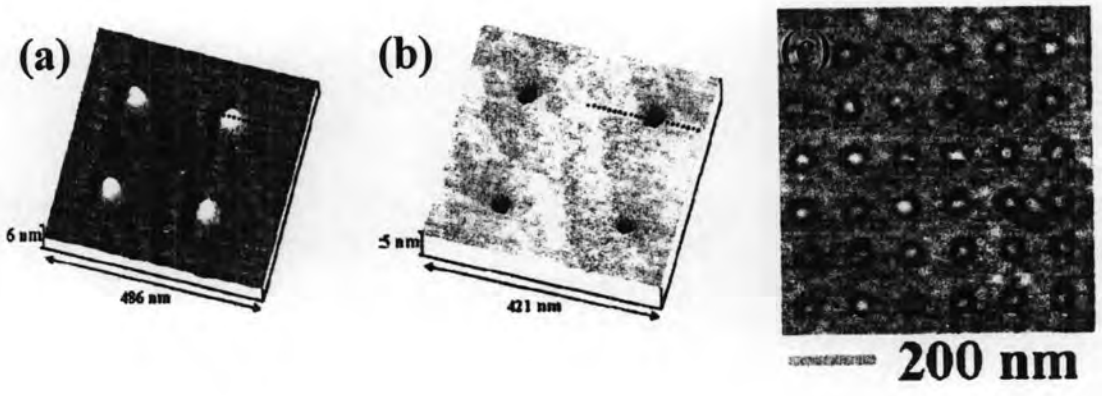

Figure 3.40 AFM images of (a) nano-oxide dots (b) nanoholes and (c) InAs QD arrays grown by droplet epitaxy (Kim et al., 2006).

Conclusion

The growth of self-assembled nanostructures is studied by MBE growth technique. The lattice mismatched epitaxy for InAs/GaAs have been summarized. The effects of strain on epitaxial growth are discussed. Defects and dislocation properties are discussed in order to understand strain mechanism in strained layer heteroepitaxy.

Studies of the ordered QDs for different growth methods are reviewed. With the basic knowledge of chapter 3, next chapter will present the laterally aligned QDs on strain relaxed layers.